



## Article

# Nanomaterial with Core–Shell Structure Composed of $\{P_2W_{18}O_{62}\}$ and Cobalt Homobenzotrizoate for Supercapacitors and $H_2O_2$ -Sensing Applications

Lanyue Zhang<sup>1</sup>, Shan Di<sup>1</sup>, Hong Lin<sup>1,\*</sup>, Chunmei Wang<sup>1</sup>, Kai Yu<sup>1,2</sup>, Jinghua Lv<sup>1</sup>, Chunxiao Wang<sup>1</sup> and Baibin Zhou<sup>1,2,\*</sup>

<sup>1</sup> Key Laboratory for Photonic and Electronic Bandgap Materials, Ministry of Education, Harbin Normal University, Harbin 150025, China

<sup>2</sup> Key Laboratory of Synthesis of Functional Materials and Green Catalysis, Colleges of Heilongjiang Province, Harbin Normal University, Harbin 150025, China

\* Correspondence: lhzcc\_love@126.com (H.L.); zhou\_bai\_bin@163.com (B.Z.)

**Abstract:** Designing and preparing dual-functional Dawson-type polyoxometalate-based metal–organic framework (POMOF) energy storage materials is challenging. Here, the Dawson-type POMOF nanomaterial with the molecular formula  $CoK_4[P_2W_{18}O_{62}]@Co_3(btc)_2$  (abbreviated as  $\{P_2W_{18}\}@Co-BTC$ ,  $H_3btc = 1,3,5$ -benzylcarboxylic acid) was prepared using a solid-phase grinding method. XRD, SEM, TEM et al. analyses prove that this nanomaterial has a core–shell structure of Co-BTC wrapping around the  $\{P_2W_{18}\}$ . In the three-electrode system, it was found that  $\{P_2W_{18}\}@Co-BTC$  has the best supercapacitance performance, with a specific capacitance of  $490.7 \text{ F g}^{-1}$  ( $1 \text{ A g}^{-1}$ ) and good stability, compared to nanomaterials synthesized with different feedstock ratios and two precursors. In the symmetrical double-electrode system, both the power density ( $800.00 \text{ W kg}^{-1}$ ) and the energy density ( $11.36 \text{ Wh kg}^{-1}$ ) are greater. In addition, as the electrode material for the  $H_2O_2$  sensor,  $\{P_2W_{18}\}@Co-BTC$  also exhibits a better  $H_2O_2$ -sensing performance, such as a wide linear range ( $1.9 \mu\text{M}$ – $1.67 \text{ mM}$ ), low detection limit ( $0.633 \mu\text{M}$ ), high selectivity, stability (92.4%) and high recovery for the detection of  $H_2O_2$  in human serum samples. This study provides a new strategy for the development of Dawson-type POMOF nanomaterial compounds.

**Keywords:** Dawson-type polyoxometalates; 1,3,5-benzylcarboxylic acid; core–shell structure; supercapacitor;  $H_2O_2$  sensing



**Citation:** Zhang, L.; Di, S.; Lin, H.; Wang, C.; Yu, K.; Lv, J.; Wang, C.; Zhou, B. Nanomaterial with Core–Shell Structure Composed of  $\{P_2W_{18}O_{62}\}$  and Cobalt Homobenzotrizoate for Supercapacitors and  $H_2O_2$ -Sensing Applications. *Nanomaterials* **2023**, *13*, 1176. <https://doi.org/10.3390/nano13071176>

Academic Editors: Sergio Brutti and Jung Woo Lee

Received: 4 January 2023

Revised: 1 March 2023

Accepted: 23 March 2023

Published: 25 March 2023



**Copyright:** © 2023 by the authors. Licensee MDPI, Basel, Switzerland. This article is an open access article distributed under the terms and conditions of the Creative Commons Attribution (CC BY) license (<https://creativecommons.org/licenses/by/4.0/>).

## 1. Introduction

With the ever-changing energy types and demands, how to better develop and utilize clean energy and design devices for better energy storage has become the current research hotspot. Due to their lengthy cycle life and high specific capacitance, extensive attention scholars have been attracted to supercapacitors [1,2]. As a green energy storage device, they can be divided into pseudocapacitors (PCs) and electric double-layer capacitors (EDLCs) according to the charge storage mechanism [3,4]. Electrode materials are at the heart of the research on these two types of supercapacitors. The electrode materials of PCs are mostly metal oxides [5], such as  $RuO_2$  [6],  $MnO_2$  [7],  $WO_3$  [8] and  $MoO_3$  [9], which are characterized by the ability to store charges on the electrode surface through redox reactions, in addition to the formation of electric double-layers through ion adsorption. They have the advantages of a high specific capacitance and high energy density. EDLCs are mainly made of carbon materials, which have the characteristics of a good cycle stability and high electrical conductivity [10–12]. Supercapacitors are limited in practical applications due to defects such as a poor PC rate performance, short cycle life and low EDLC specific capacitance [13]. Therefore, developing electrode materials with excellent properties and satisfactory practical applications is a challenging task.

Polyoxometalates (POMs) are clusters of various metal oxides with promising applications in many fields, such as electrochemistry [14] and medicine [15]. Recently, POMs have been regarded as one of the most promising materials for supercapacitors and H<sub>2</sub>O<sub>2</sub>-sensing electrodes due to their reversible redox activity, high charge density and electron storage capacity. In the existing literature, hybrids of Keggin-type POMs have been studied more [16–22]. However, Dawson-type POMs are rarely reported. For example, Ma [23] group synthesized a novel coordination polymer (H<sub>2</sub>bpe)(Hbpe)<sub>2</sub>{[Cu(pzta)(H<sub>2</sub>O)][P<sub>2</sub>W<sub>18</sub>O<sub>62</sub>]}·5H<sub>2</sub>O with good electrochemical properties using a hydrothermal method in 2017. More reports are shown in Table S1. The data in Table S1 show that Dawson POMs are widely used in photocatalysis and sensing, and the highly negatively charged, oxygen-rich surface of Dawson-type POMs can enhance the charge separation and electron transmission efficiency [24–26], which is beneficial for improving the performance of supercapacitors and H<sub>2</sub>O<sub>2</sub> sensors. In recent years, our group has reported several cases of Dawson-type POM compounds with an excellent supercapacitors performance synthesized using the hydrothermal method [27–31]. However, its large solubility in electrolytes or water and low intrinsic conductivity hinder its practical application as a solid electrode material in supercapacitors and sensing. As a new type of functional material, metal–organic frameworks (MOFs) have the advantages of chemical sustainability and a high specific surface area, and their organic ligands and metal ion properties have a great impact on the adaptability of POMs [32,33]. Therefore, immobilizing POMs on MOFs to prepare POMOFs is a good approach to improve electronic conductivity and reduce solubility to optimize their performance as solid electrode materials [34]. Dawson-type POMOFs are usually obtained using the hydrothermal method [35–37], but the difficulty of repetition and low yield limit their large-scale application. The grinding method is a simple and efficient method [38]. Thus, we propose a solid-phase grinding method to synthesize POMOFs, which solves the problems present in the hydrothermal method [39].

Green and pollution-free oxidant-H<sub>2</sub>O<sub>2</sub> is widely used in production and life. High levels of H<sub>2</sub>O<sub>2</sub> in the environment will have some harmful effects on the human body, such as causing gene damage. It is significant to realize the rapid and accurate detection of H<sub>2</sub>O<sub>2</sub> content. Electrochemical detection methods have attracted attention due to their high sensitivity and low cost, and the main sensor materials used are nanocomposite materials and enzymes. Nevertheless, the poor stability of the two materials limits their applications [40]. Finding suitable sensor materials is one of the research hotspots of H<sub>2</sub>O<sub>2</sub> sensors.

On this basis, the core–shell structure {P<sub>2</sub>W<sub>18</sub>}@Co-BTC was synthesized using [P<sub>2</sub>W<sub>18</sub>O<sub>62</sub>]<sup>6−</sup>, Co<sup>2+</sup> and H<sub>3</sub>btc ligands. The synthesis was considered as follows: (I) the surface of [P<sub>2</sub>W<sub>18</sub>O<sub>62</sub>]<sup>6−</sup> has many negatively charged oxygen atoms and it is easy for it to cooperate with transition metals to form new structures; (II) the various coordination modes of transition metal Co<sup>2+</sup> give it a better performance in supercapacitors; (III) It is easy to coordinate H<sub>3</sub>btc with transition metals, with various coordination modes and binding sites. Based on the above considerations, a core–shell structure with Co-BTC as the shell wrapped on the {P<sub>2</sub>W<sub>18</sub>} core was synthesized using the solid-phase grinding method. Notably, the synergy between the core ({P<sub>2</sub>W<sub>18</sub>}) and the shell (Co-BTC) enhances the electronic conductivity and stability of the nanomaterial, and also provides a larger specific surface area and an abundance of active sites.

In this paper, we performed a series of characterizations on the nanomaterials, such as IR, XRD, SEM, TEM, XPS, etc. In the three-electrode system of supercapacitors, the performances of the target nanomaterial and precursors were compared, and the performance gap between nickel foam (NF) and carbon cloth (CC) as collectors and the synthesis ratio of nanomaterials were discussed. In addition, the symmetrical double-electrode test and H<sub>2</sub>O<sub>2</sub> sensing test were performed.

## 2. Materials and Methods

### 2.1. Synthesis of $\text{CoK}_4[\text{P}_2\text{W}_{18}\text{O}_{62}]$

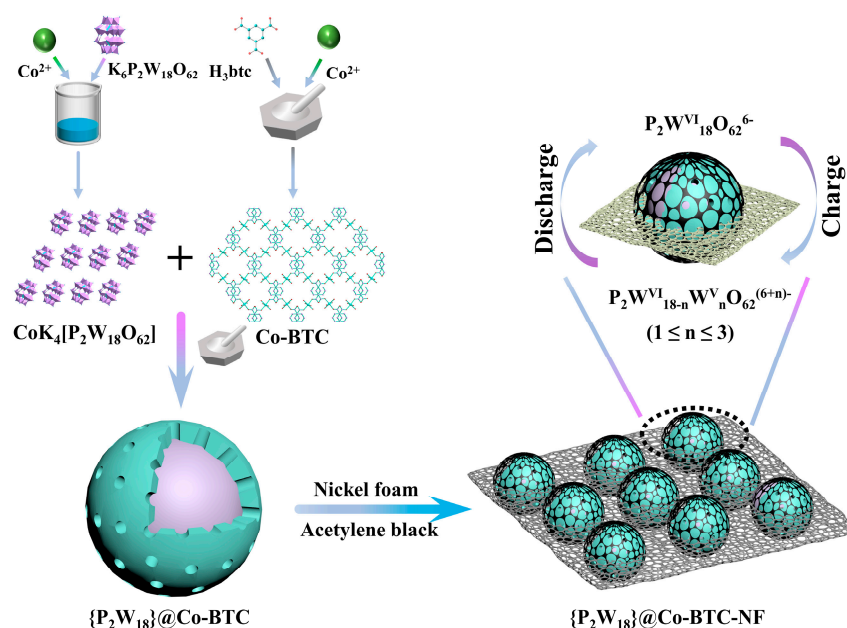
$\text{K}_6[\text{P}_2\text{W}_{18}\text{O}_{62}] \cdot 15\text{H}_2\text{O}$  (0.15 mmol, see Supplementary Information for its synthesis) and  $\text{Co}(\text{NO}_3)_2$  (0.41 mmol) were dissolved in 10 mL of distilled water. The pH was adjusted to 4.5 with 0.1 M NaOH, and, after stirring for 6 h at room temperature, the mixture was evaporated, concentrated, crystallized and dried at 60 °C for 24 h, obtaining  $\text{CoK}_4[\text{P}_2\text{W}_{18}\text{O}_{62}]$ .

### 2.2. Synthesis of $\text{Co}_3(\text{btc})_2$

$\text{H}_3\text{btc}$  (0.49 mmol) and  $\text{Co}(\text{NO}_3)_2$  (0.41 mmol) were weighed in a mortar, 0.5 mL anhydrous ethanol was added every hour, and the sample was ground with approximately 2~3 kg force for 3 h. The sample completely changed to light pink and was dried to obtain  $\text{Co}_3(\text{btc})_2$  (abbreviated as Co-BTC).

### 2.3. Synthesis of $\text{CoK}_4[\text{P}_2\text{W}_{18}\text{O}_{62}]@\text{Co-BTC}$

The  $\text{CoK}_4[\text{P}_2\text{W}_{18}\text{O}_{62}]$  (0.10 mmol) and Co-BTC (0.30 mmol) were mixed and 1 mL of anhydrous ethanol was added every hour for 2 h. Then, the sample was ground with approximately 2~3 kg force for 2 h. The sample color gradually changed to dark pink, and was then washed three times with anhydrous ethanol and separated by centrifugation, followed by being dried in an oven at 60 °C for 24 h to obtain the nanomaterial  $\text{CoK}_4[\text{P}_2\text{W}_{18}\text{O}_{62}]@\text{Co-BTC}$  (abbreviated as  $\{\text{P}_2\text{W}_{18}\}@\text{Co-BTC}$ ). In the same method, nanomaterials with feeding ratio of 1:1, 1:2 and 1:4 from  $\text{CoK}_4[\text{P}_2\text{W}_{18}\text{O}_{62}]$  to Co-BTC were synthesized, expressed as  $\{\text{P}_2\text{W}_{18}\}@\text{Co-BTC-1}$ ,  $\{\text{P}_2\text{W}_{18}\}@\text{Co-BTC-2}$  and  $\{\text{P}_2\text{W}_{18}\}@\text{Co-BTC-3}$ , respectively. For the synthesis strategy, see Scheme 1.



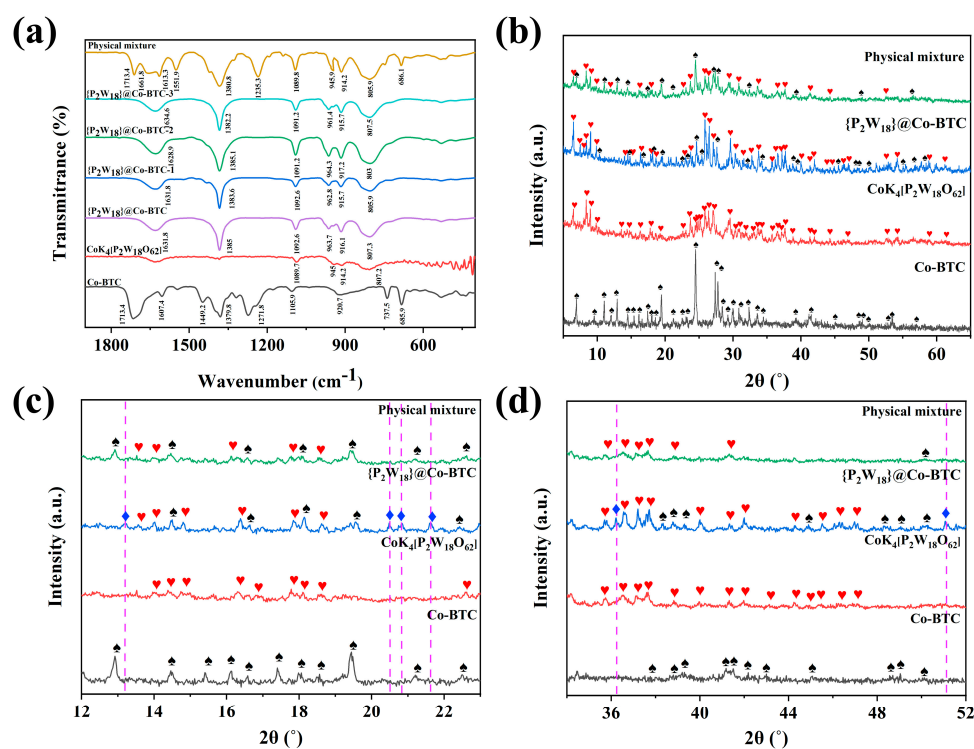
**Scheme 1.** The synthesis strategies of  $\{\text{P}_2\text{W}_{18}\}@\text{Co-BTC}$  nanomaterial and  $\{\text{P}_2\text{W}_{18}\}@\text{Co-BTC-NF}$  and the working mechanism of  $\{\text{P}_2\text{W}_{18}\}@\text{Co-BTC-NF}$  in supercapacitors are illustrated.

## 3. Results and Discussion

### 3.1. Characterization

In order to determine the structure of the nanomaterial, a series of characterizations (IR, XRD, TG, SEM, etc.) were performed on the  $\{\text{P}_2\text{W}_{18}\}@\text{Co-BTC}$ . Figure 1a (part) and Figure S1a (ensemble) show the IR diagram of Co-BTC,  $\text{CoK}_4[\text{P}_2\text{W}_{18}\text{O}_{62}]$ ,  $\{\text{P}_2\text{W}_{18}\}@\text{Co-BTC-n}$  ( $n = 0, 1\sim 3$ ) and the physical mixture. The absorption peak near  $3400\text{ cm}^{-1}$  belongs to the O-H peak of  $\text{H}_2\text{O}$ . The absorption peaks at  $1089.7\text{ cm}^{-1}$ ,  $945.0\text{ cm}^{-1}$ ,  $914.2\text{ cm}^{-1}$

and  $807.2\text{ cm}^{-1}$  in  $\text{CoK}_4[\text{P}_2\text{W}_{18}\text{O}_{62}]$  correspond to the  $\nu_{\text{as}}(\text{P-O}_a)$ ,  $\nu_{\text{as}}(\text{W-O}_t)$ ,  $\nu_{\text{as}}(\text{W-O}_b\text{-W})$  and  $\nu_{\text{as}}(\text{W-O}_c\text{-W})$ . Compared with  $\text{K}_6[\text{P}_2\text{W}_{18}\text{O}_{62}]$  [41], the introduction of  $\text{Co}^{2+}$  induces the shift in characteristic peaks, explaining the synthesis of  $\text{CoK}_4[\text{P}_2\text{W}_{18}\text{O}_{62}]$ . For Co-BTC, the absorption peak at  $685.9\text{ cm}^{-1}$  belongs to the stretching vibration of the Co-O [42]. The absorption peaks exhibited at  $1379.8\text{ cm}^{-1}$  and  $1607.4\text{ cm}^{-1}$  belong to the vibrational characteristic peaks of asymmetric  $\nu_{\text{as}}(\text{C-O})$  and symmetric  $\nu_{\text{as}}(\text{C-O})$  in the carboxyl groups, these characteristics peaks being consistent with those of  $\text{H}_3\text{btc}$  [43]. In addition, the absorption peak at  $1714.0\text{ cm}^{-1}$  generated by the vibration of the non-ionized carboxyl group indicates that  $\text{Co}^{2+}$  binds to BTC instead of H, showing that Co-BTC can be successfully synthesized by the solid-phase grinding method. The four characteristic peaks at  $1092.6\text{ cm}^{-1}$ ,  $962.8\text{ cm}^{-1}$ ,  $915.7\text{ cm}^{-1}$  and  $805.9\text{ cm}^{-1}$  in  $\{\text{P}_2\text{W}_{18}\}\text{@Co-BTC}$  belong to the  $\nu_{\text{as}}(\text{P-O}_a)$ ,  $\nu_{\text{as}}(\text{W-O}_t)$ ,  $\nu_{\text{as}}(\text{W-O}_b\text{-W})$  and  $\nu_{\text{as}}(\text{W-O}_c\text{-W})$  in  $\text{CoK}_4[\text{P}_2\text{W}_{18}\text{O}_{62}]$ , respectively. The  $\nu_{\text{as}}(\text{W-O}_t)$  moved by  $17.8\text{ cm}^{-1}$ , indicating that the terminal oxygen of  $\{\text{P}_2\text{W}_{18}\}$  has a strong coordination effect with Co-BTC. Furthermore, the two peaks at  $1631.8\text{ cm}^{-1}$  and  $1385.0\text{ cm}^{-1}$  are asymmetric and symmetric  $\nu_{\text{as}}(\text{C-O})$  peaks in Co-BTC, confirming the synthesis of  $\{\text{P}_2\text{W}_{18}\}\text{@Co-BTC}$ . The physical mixture contains characteristic peaks of  $\text{CoK}_4[\text{P}_2\text{W}_{18}\text{O}_{62}]$  and Co-BTC. Compared with the IR spectrum of  $\{\text{P}_2\text{W}_{18}\}\text{@Co-BTC}$ , it is clear that the peaks of Co-BTC and  $\text{CoK}_4[\text{P}_2\text{W}_{18}\text{O}_{62}]$  in the physical mixture have no offset. Moreover, the characteristic peaks of  $\{\text{P}_2\text{W}_{18}\}\text{@Co-BTC-1-3}$  clearly illustrate their successful synthesis, but with different peak intensities compared to  $\{\text{P}_2\text{W}_{18}\}\text{@Co-BTC}$ .



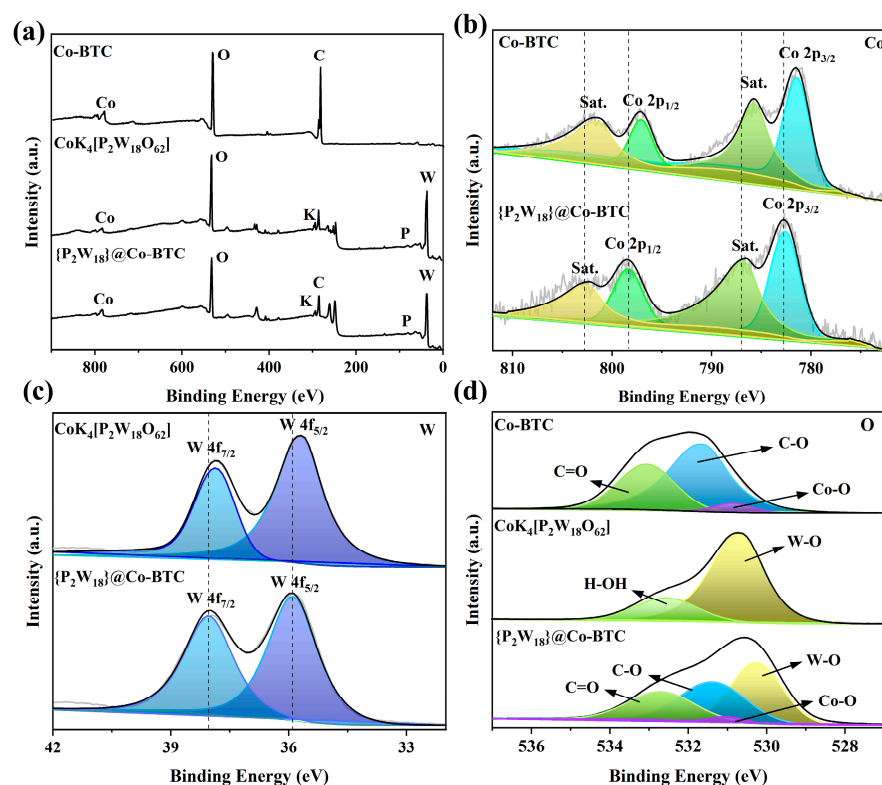
**Figure 1.** (a) The IR of Co-BTC,  $\text{CoK}_4[\text{P}_2\text{W}_{18}\text{O}_{62}]$ ,  $\{\text{P}_2\text{W}_{18}\}\text{@Co-BTC-n}$  ( $n = 0, 1\text{--}3$ ) and physical mixture; (b) the XRD of Co-BTC,  $\text{CoK}_4[\text{P}_2\text{W}_{18}\text{O}_{62}]$ ,  $\{\text{P}_2\text{W}_{18}\}\text{@Co-BTC}$  and physical mixture; (c,d) the identification of the new diffraction rays ( $\clubsuit$ ,  $\heartsuit$  and  $\diamondsuit$  respectively represent the characteristic peaks of Co-BTC,  $\text{CoK}_4[\text{P}_2\text{W}_{18}\text{O}_{62}]$ ,  $\{\text{P}_2\text{W}_{18}\}\text{@Co-BTC}$ ).

Figure 1b shows the XRD patterns of Co-BTC,  $\text{CoK}_4[\text{P}_2\text{W}_{18}\text{O}_{62}]$ ,  $\{\text{P}_2\text{W}_{18}\}\text{@Co-BTC}$  and the physical mixture. The diffraction peaks of the physical mixture are in perfect agreement with the  $\text{CoK}_4[\text{P}_2\text{W}_{18}\text{O}_{62}]$  and Co-BTC.  $\{\text{P}_2\text{W}_{18}\}\text{@Co-BTC-n}$  contains characteristic peaks of  $\text{CoK}_4[\text{P}_2\text{W}_{18}\text{O}_{62}]$  and Co-BTC, where the peaks are slightly shifted to match the degree of  $\text{CoK}_4[\text{P}_2\text{W}_{18}\text{O}_{62}]$ , which is higher. We guessed that the diffraction peaks of  $\text{CoK}_4[\text{P}_2\text{W}_{18}\text{O}_{62}]$  in  $\{\text{P}_2\text{W}_{18}\}\text{@Co-BTC}$  should mask some peaks of Co-BTC (Figure S1b). In

addition,  $\{P_2W_{18}\}@Co-BTC$  produced new diffraction peaks at  $13.22^\circ$ ,  $20.48^\circ$ ,  $20.84^\circ$ ,  $21.64^\circ$ ,  $36.24^\circ$  and  $51.06^\circ$  (in Figure 1c,d), determining that  $CoK_4[P_2W_{18}O_{62}]$  cooperated with Co-BTC to form the target synthesis product [44]. New phases also exist in  $\{P_2W_{18}\}@Co-BTC-1-3$  (◆ in Figure S1b), confirming that  $\{P_2W_{18}\}@Co-BTC-1-3$  are all synthesized as new nanomaterials. Moreover,  $\{P_2W_{18}\}@Co-BTC$  produced more new phases and sharper peaks, illustrating that this ratio (1:3) has good crystallinity and is the best ratio for the synthesis of nanomaterials.

XPS further verified the existence and valence of the constituent elements of the nanomaterial. The XPS test results of  $\{P_2W_{18}\}@Co-BTC$ ,  $CoK_4[P_2W_{18}O_{62}]$  and Co-BTC are shown in Figures S2–S4 (see supplementary information for discussion). Figure 2a shows a full spectral comparison of  $CoK_4[P_2W_{18}O_{62}]$ , Co-BTC and  $\{P_2W_{18}\}@Co-BTC$ , showing the presence of each element in the three compounds, confirming the purity of the compounds. In the  $Co_{2p}$  spectrum of  $\{P_2W_{18}\}@Co-BTC$  (Figure S2d), two major peaks of  $Co_{2p_{1/2}}$  (798.4 eV) and  $Co_{2p_{3/2}}$  (782.6 eV) along with their corresponding satellite peaks (802.4 eV and 786.6 eV) are exhibited. According to related research [45], the signal of 782.6 eV on the low-binding-energy side is assigned to Co(II), which means that the main existing state of Co in  $\{P_2W_{18}\}@Co-BTC$  is the Co(II) oxidation state. Compared with the four peaks of Co-BTC, the four characteristic peaks of  $\{P_2W_{18}\}@Co-BTC$  shifted towards the high-binding-energy side, and the maximum displacement value was approximately 5 eV (Figure 2b). Figure S2e shows the  $\{P_2W_{18}\}@Co-BTC$   $K_{2p}$  spectrum, showing two main peaks around 293 eV ( $K_{2p_{1/2}}$ ) and 295.9 eV ( $K_{2p_{3/2}}$ ). Based on the peak values of  $K_{2p}$ , the main valence state of K is +1 valence [46]. Similarly, the spectrum of  $W_{4f}$  (Figure S2c) displayed two peaks at 38 eV ( $W_{4f_{5/2}}$ ) and 35.9 eV ( $W_{4f_{7/2}}$ ), corresponding to the W–O bonds observed in W(VI) [41]. The  $P_{2p}$  spectrum (Figure S2b) shows the peaks at 133.7 eV ( $P_{2p_1}$ ), corresponding to P(V). The existence of  $P_{2p}$  and  $W_{4f}$  proves that  $\{P_2W_{18}\}@Co-BTC$  has retained the original framework of  $\{P_2W_{18}\}$ . Notably,  $W_{4f_{5/2}}$  and  $W_{4f_{7/2}}$  in the  $\{P_2W_{18}\}@Co-BTC$  underwent a positive shift of  $\sim 0.3$  eV compared to the  $W_{4f}$  spectrum in  $CoK_4[P_2W_{18}O_{62}]$  (Figure 2c).  $\{P_2W_{18}\}@Co-BTC$  has four  $O_{1s}$  peaks—530.28 eV (W–O), 530.98 eV (Co–O), 531.38 eV (C–O) and 532.68 eV (C=O)—and it can be seen from Figure 2d that the  $O_{1s}$  peak of  $\{P_2W_{18}\}@Co-BTC$  showed a slight low-energy shift compared with  $CoK_4[P_2W_{18}O_{62}]$  and Co-BTC. Combined with the peak migration results of Co, O and W in  $\{P_2W_{18}\}@Co-BTC$ , we speculate that the electron cloud of O in  $CoK_4[P_2W_{18}O_{62}]$  overlapped with the electron cloud of Co in Co-BTC, forming an interaction that weakens the force of O and W, resulting in the peak migration of Co and O being greater than that of W. These results prove the strong interaction between Co-BTC and  $\{P_2W_{18}\}$ , implying the successful synthesis of  $\{P_2W_{18}\}@Co-BTC$  [47,48]. Among these elements, carbon ( $C_{1s}$ ) can also demonstrate the successful synthesis of  $\{P_2W_{18}\}@Co-BTC$ , where we found two peaks of C–C/C=C and C=O at 284.6 eV and 288.9 eV (Figure S2g), again confirming the presence of Co-BTC in the title nanomaterial [49]. Combining IR, XRD and XPS can clearly confirm that  $\{P_2W_{18}\}@Co-BTC$  can be successfully synthesized using the solid-phase grinding method.

The TG of  $\{P_2W_{18}\}@Co-BTC$  gives the main three steps of weight loss (Figure S5). The first and second step of weight loss is between 30–400 °C, and the weight loss rate is approximately 17.85%, which belongs to the loss of water molecules on the surface and the decomposition of Co-BTC [50]. The third step of weight loss between 400–600 °C is the decomposition of  $\{P_2W_{18}\}$  in  $\{P_2W_{18}\}@Co-BTC$ , with a weight loss rate of approximately 4.92%. The final compound is decomposed into metal oxides ( $Co_3O_4$ ,  $K_2O$ ), tungsten carbide ( $W_2C$ ) and C, similar to the literature [51]. Combining the ICP-MS (Table S2), TG and XPS results, the molecular formula of the nanomaterial was calculated as  $CoK_4[P_2W_{18}O_{62}]\@Co_3(btc)_2$ .



**Figure 2.** The full XPS (a) and  $O_{1s}$  spectra (d) of  $\{P_2W_{18}\}@Co-BTC$ ,  $CoK_4[P_2W_{18}O_{62}]$  and  $Co-BTC$ ; (b)  $Co_{2p}$  spectra of  $\{P_2W_{18}\}@Co-BTC$  and  $Co-BTC$ ; (c)  $W_{4f}$  spectra of  $\{P_2W_{18}\}@Co-BTC$  and  $CoK_4[P_2W_{18}O_{62}]$ .

$\{P_2W_{18}\}@Co-BTC$  is in the shape of a cuboid, with lengths of 3.13  $\mu m$  and 2.86  $\mu m$  and a width and height of approximately 2.78  $\mu m$  and 0.82  $\mu m$ , respectively (Figure 3a). EDS (Figure S6a) and EDX show the even distribution of C, O, K (Figure S6b–d), P, W and Co (Figure 3b–d) elements in  $\{P_2W_{18}\}@Co-BTC$ . Similarly, Figures S7 and S8 show the morphology of  $CoK_4[P_2W_{18}O_{62}]$  and  $Co-BTC$  as irregular massive deposits and rod-like structures, respectively, and also show the uniform distribution of each element. From the above results, in the process of combining  $CoK_4[P_2W_{18}O_{62}]$  and  $Co-BTC$  through intermolecular forces, the coordination balance of BTC and  $Co^{2+}$  changes, resulting in the deformation of  $Co-BTC$ , which makes the morphology of the nanomaterial similar to that of  $CoK_4[P_2W_{18}O_{62}]$ , forming a core–shell structure with  $CoK_4[P_2W_{18}O_{62}]$  as the core and  $Co-BTC$  as the shell. The EDS results show that the molar ratio of  $K:P = 1.85:1$  in  $\{P_2W_{18}\}@Co-BTC$  and  $K:P = 1.86:1$  in  $CoK_4[P_2W_{18}O_{62}]$  was close, again verifying the purity of  $\{P_2W_{18}\}@Co-BTC$ . The TEM image (Figure 3e) and lattice fringe pattern (Figure 3f) of  $\{P_2W_{18}\}@Co-BTC$  also confirm the conjecture. Figure 3f shows that the spacings of the lattice fringe correspond to 0.295 nm ( $Co-BTC$ ) and 0.251 nm ( $\{P_2W_{18}\}$ ), and that  $Co-BTC$  can be found wrapped uniformly around the  $\{P_2W_{18}\}$  surface. These results demonstrate that  $\{P_2W_{18}\}$  is encapsulated within the metal–organic framework, providing a large specific surface area for the target product.

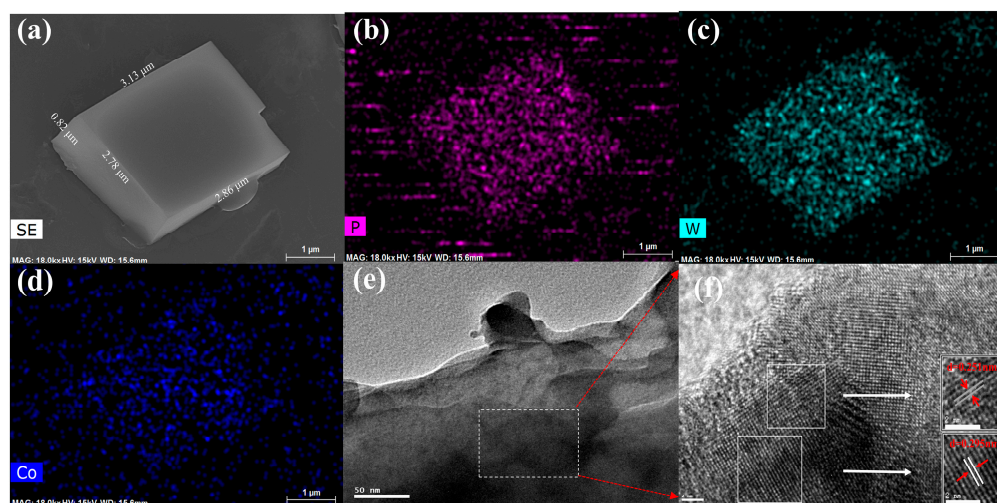


**Figure 3.** SEM images (a), mapping of P (b), W (c) and Co (d), TEM image (e) and the crystal plane analysis diagram (f) of  $\{P_2W_{18}\}@Co-BTC$ .

The  $N_2$  adsorption and desorption isotherms of Co-BTC,  $CoK_4[P_2W_{18}O_{62}]$  and  $\{P_2W_{18}\}@Co-BTC$  were tested, and the isotherms were in the shape of hysteresis loops (Figure S9a) and pore size distribution maps (Figure S9b). The specific surface area and pore size of the nanomaterials were calculated using the Barrett–Joyner–Halenda method, the specific surface areas were  $12.302\text{ m}^2\text{ g}^{-1}$ ,  $11.499\text{ m}^2\text{ g}^{-1}$  and  $14.45\text{ m}^2\text{ g}^{-1}$  and the pore sizes were 2.124 nm, 2.252 nm and 3.895 nm. As can be seen from the calculations, compared with  $CoK_4[P_2W_{18}O_{62}]$ , the nanomaterials synthesized using the solid-phase grinding method not only increase the specific surface area, making the electrolyte easier to infiltrate, but also increase the pore size and improve the diffusion rate of electrolyte ions [52,53].

### 3.2. Supercapacitors Performance

Combined with the characterization results, one of the advantages of synthesizing the nanomaterial using the solid-phase grinding method is the increased specific surface area, indicating that the material has promise for use as an electrochemical electrode material and improves the electrochemical performance. The performance of the nanomaterial three-electrode supercapacitor was tested under the conditions that the electrolyte was 1 M  $Na_2SO_4$  and nickel foam was the collector.

In order to determine the optimal ratio of nanomaterials, the effect of Co-BTC on the electrochemical performance was investigated by comparing the  $\{P_2W_{18}\}@Co-BTC-n$  ( $n = 0, 1\sim 3$ ) of CV and GCD. Figure 4a,b are the CV and GCD comparison diagrams of the four nanomaterials. Figure 4a shows that the ideal molar ratio of  $CoK_4[P_2W_{18}O_{62}]$  to Co-BTC is 1:3, and that the  $\{P_2W_{18}\}@Co-BTC$  area is the largest. According to Equation (S1), the specific capacitances of the nanomaterials with different ratios are  $298.5\text{ F g}^{-1}$ ,  $363\text{ F g}^{-1}$ ,  $490.7\text{ F g}^{-1}$  and  $171.6\text{ F g}^{-1}$ , respectively, which may be related to the degree of synergy between Co-BTC and  $CoK_4[P_2W_{18}O_{62}]$  in  $\{P_2W_{18}\}@Co-BTC$  and the characteristics of MOF itself. The higher the content of Co-BTC, the more abundant channels and micropores of MOF, the greater the synergy with the  $CoK_4[P_2W_{18}O_{62}]$ , the greater the number of active sites of  $\{P_2W_{18}\}@Co-BTC$  and the greater the specific capacitance. Moreover, the GCD of 1:3 ( $490.7\text{ F g}^{-1}$ ) is significantly greater than 1:4 ( $171.6\text{ F g}^{-1}$ ) due to the unbalance synergy between  $\{P_2W_{18}\}$  and Co-BTC. Hence, it can be inferred that the Co-BTC in  $\{P_2W_{18}\}@Co-BTC$  has a positive effect on its electrochemical performance, among which the nanomaterial synthesized at 1:3 performs the best.

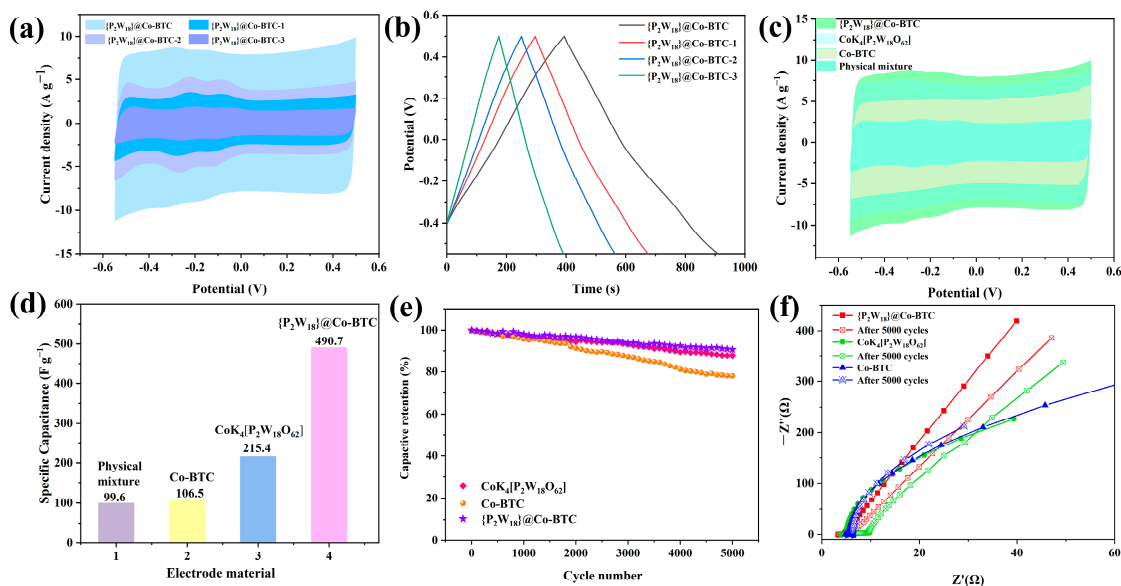


**Figure 4.** Comparison diagram of CV (a) and GCD (b) for  $\{P_2W_{18}\}@Co-BTC-n$  ( $n = 0, 1-3$ ); (c) the CV comparison chart of  $\{P_2W_{18}\}@Co-BTC$ ,  $CoK_4[P_2W_{18}O_{62}]$ ,  $Co-BTC$  and physical mixture in  $40\text{ mV s}^{-1}$ ; (d) the specific capacitance of  $\{P_2W_{18}\}@Co-BTC$ ,  $CoK_4[P_2W_{18}O_{62}]$ ,  $Co-BTC$  and physical mixture at  $1\text{ A g}^{-1}$ ; (e) cycling stabilities of  $\{P_2W_{18}\}@Co-BTC$ ,  $CoK_4[P_2W_{18}O_{62}]$  and  $Co-BTC$ ; (f) the EIS of  $\{P_2W_{18}\}@Co-BTC$ ,  $CoK_4[P_2W_{18}O_{62}]$  and  $Co-BTC$  before and after 5000 cycles of three-electrode system.

To further investigate the supercapacitive properties of the synthesized nanomaterials under optimal conditions, the electrochemical properties of  $\{P_2W_{18}\}@Co-BTC$ ,  $CoK_4[P_2W_{18}O_{62}]$ ,  $Co-BTC$  and the physical mixture were tested. Figure S10a shows the CV curve of  $\{P_2W_{18}\}@Co-BTC$ , showing two pairs of weak redox peaks, representing the redox process of the W atom in the  $[P_2W_{18}O_{62}]^{6-}$  polyoxoanion [54]. At the same scan speed, the areas of the CV curve of  $\{P_2W_{18}\}@Co-BTC$ ,  $CoK_4[P_2W_{18}O_{62}]$ ,  $Co-BTC$  and the physical mixture decrease in turn, and the pseudocapacitance of  $\{P_2W_{18}\}@Co-BTC$  is the largest, credited to the synergistic effect of the  $CoK_4[P_2W_{18}O_{62}]$  and  $Co-BTC$  in the nanomaterial (Figure 4c). Furthermore, the CV curves of the  $CoK_4[P_2W_{18}O_{62}]$  and  $Co-BTC$  proved their good rate performance (Figure S10b,c). Furthermore, the anodic peak current of  $\{P_2W_{18}\}@Co-BTC$ ,  $CoK_4[P_2W_{18}O_{62}]$  and  $Co-BTC$  showed a linear relationship with the scan rate ( $5-40\text{ mV s}^{-1}$ ), indicating that all three species exhibit surface-controlled redox reactions, proving that they are all capacitive materials (Figure S10d) [55]. Figure S10e is the GCD comparison curve of  $CoK_4[P_2W_{18}O_{62}]$ ,  $Co-BTC$ , the physical mixture and  $\{P_2W_{18}\}@Co-BTC$ . According to Equation (S1), at a current density of  $1\text{ A g}^{-1}$ , the specific capacitances of the four compounds were  $215.4\text{ F g}^{-1}$ ,  $106.5\text{ F g}^{-1}$ ,  $99.6\text{ F g}^{-1}$  and  $490.7\text{ F g}^{-1}$  (Figure 4d). The specific capacitance of  $\{P_2W_{18}\}@Co-BTC$  is superior to that of a physical mixture of the same proportions because of the synergy between  $CoK_4[P_2W_{18}O_{62}]$  and  $Co-BTC$  in the POMOF nanomaterial. Meanwhile, the specific capacitance of  $\{P_2W_{18}\}@Co-BTC$  ( $490.7\text{ F g}^{-1}$ ) is higher than those reported in many literatures (see Table S3). This result may be related to the excellent electron conduction and more electron transfer pathways provided by the core-shell structure of  $\{P_2W_{18}\}@Co-BTC$ . From Figure 4b, the compound presence of a small  $iR$  drop can be attributed to the synergistic effect of  $\{P_2W_{18}\}$  and  $Co-BTC$ , and can provide a fast transport route for electrons and ions [56,57].

In order to evaluate whether  $\{P_2W_{18}\}@Co-BTC$ ,  $CoK_4[P_2W_{18}O_{62}]$  and  $Co-BTC$  have good stability, the capacitance retention rates of the three nanomaterials at  $10\text{ A g}^{-1}$  and 5000 charge-discharge cycles were tested, and the test results were 90.6%, 78.1% and 87.8%, respectively (Figure 4e). The  $CoK_4[P_2W_{18}O_{62}]$  anion in  $\{P_2W_{18}\}@Co-BTC$  has a reversible multi-electron transfer reaction, and the highly negatively charged oxygen atom on its surface increases its interaction effect with  $Co-BTC$ , thereby improving the stability of the entire structure [58]. Meanwhile, to further understand whether the nanomaterials

have the potential to serve as electrodes with a good performance, EIS measurements before and after 5000 cycles were carried out, and the  $R_s$  of the three nanomaterials was calculated.  $R_s$  is the equivalent series resistance, and is a sum of the electrode, the contact resistance between the active material and the collector, and the electrolyte resistance [59]. Figure 4f and Figure S10f show the EIS spectra of the three nanomaterials before and after cycling and their magnified images in the high-frequency region, where the  $R_s$  of  $\{P_2W_{18}\}@Co-BTC$ ,  $CoK_4[P_2W_{18}O_{62}]$  and  $Co-BTC$  before cycling is 3.29  $\Omega$ , 3.96  $\Omega$  and 4.78  $\Omega$ , respectively, and the  $R_s$  after cycling is 3.75  $\Omega$ , 4.26  $\Omega$  and 5.48  $\Omega$ . In the low-frequency region, the slope of the  $\{P_2W_{18}\}@Co-BTC$  curve before and after the cycle is the largest, meaning that the  $R_{ct}$  of  $\{P_2W_{18}\}@Co-BTC$  before and after the cycle is the smallest [60]. These results demonstrate that  $\{P_2W_{18}\}@Co-BTC$  has ideal capacitive properties and a good rate capability, indicating that the POMOF nanomaterial with a core-shell structure reduces the dissolution of  $CoK_4[P_2W_{18}O_{62}]$  in the electrolyte and plays a positive role in the electrochemical double-layer capacitance.

In order to study the effect of different collectors on the performance of  $\{P_2W_{18}\}@Co-BTC$  supercapacitors, the capacitive behavior of carbon cloth collectors was tested. Figure S11a,b show that carbon cloth has stronger pseudocapacitive properties than nickel foam. As the scanning rate increases, the shape of the CV curve does not change significantly, with only a slight change in the redox peak, owing to the change in the conductivity of the electrode. Figures S10a and S11c show the CV curve of  $\{P_2W_{18}\}@Co-BTC$  with nickel foam and with carbon cloth as the collector. A comparison shows that, at the same scan rate of 40  $mV s^{-1}$ , the area of the CV curve of carbon cloth is smaller than that of NF, which may be attributed to the slower polarization rate of the NF electrode, which can activate more redox active sites and improve the capacitance of  $\{P_2W_{18}\}@Co-BTC$ . Figures 5a and S11d show that the specific capacitance of  $\{P_2W_{18}\}@Co-BTC-CC$  (155.7  $F g^{-1}$ ) is smaller than  $\{P_2W_{18}\}@Co-BTC-NF$  (490.7  $F g^{-1}$ ), indicating that the NF electrode can significantly improve the discharge time of  $\{P_2W_{18}\}@Co-BTC$ , which is associated with the excellent electrical conductivity provided by the abundant pore structure of the NF electrodes. The EISs of  $\{P_2W_{18}\}@Co-BTC$  on CC and NF were also compared (Figure 5b), showing that the  $R_s$  for CC (6.43  $\Omega$ ) is larger than the  $R_s$  for NF (3.29  $\Omega$ ) due to the influence of the resistivity of different electrode materials. In addition, the slopes of  $\{P_2W_{18}\}@Co-BTC-CC$  and  $\{P_2W_{18}\}@Co-BTC-NF$  curves in the high-frequency region ( $R_{ct-CC} < R_{ct-NF}$ ) may be caused by the unique porous structure of NF, allowing it to adhere more closely to  $\{P_2W_{18}\}@Co-BTC$  and enhance the rapid charge transfer capability at the interface of electrolyte  $Na_2SO_4$  and nanomaterial NF [61,62]. Therefore, nickel foam is considered to be a more suitable electrode material for this nanomaterial.

The results show that the synthesized nanomaterial has the best performance when the collector is nickel foam and the raw material molar ratio is 1:3. To further study the value of  $\{P_2W_{18}\}@Co-BTC$  in practical application, an aqueous symmetric supercapacitor (ASS) (see Figure S12) was constructed with nickel foam as the collector. The CV, GCD, EIS and cycling under positive voltage (0~0.8 V) of the ASS were tested. The CV test (Figure 5c) displays that ASS is a double-layer capacitor. With an increase in the scan rate, the shape of the CV curve does not change significantly, with only a change in the current intensity, showing a higher scan rate capability. The GCD curves of ASS at current densities of 1, 1.5, 2, 3, 4 and 5  $A g^{-1}$  were tested and are shown in Figure 5d, and, by calculation (according to Equation (S2)), the maximum specific capacitance (130.5  $F g^{-1}$ ) of ASS can be obtained at 1  $A g^{-1}$ . The capacitance retention rate of ASS is 84.7% after 5000 cycles of charge and discharge at 10  $A g^{-1}$  (Figure 5e). To further understand the electrochemical performance of ASS in practical applications, electrochemical impedance measurements were carried out (Figure S13). The internal resistances ( $R_s$ ) of ASS before and after cycling were 7.7  $\Omega$  and 8.7  $\Omega$ , respectively, and the resistance increased slightly after cycling, indicating that the electronic conductivity of the electrode decreased slightly. In the low-frequency region, the slope of the curve is close to 45°, indicating that ASS has relatively excellent  $R_{ct}$  and electrochemical properties that are inseparable from the special core-shell structure of

POMOF. Meanwhile, the calculated power density of ASS is  $800.00 \text{ W kg}^{-1}$  and the energy density is  $11.36 \text{ Wh kg}^{-1}$  (according to Equations (S3)–(S4)), which is higher than many previous reports (Figure 5f) [32,38,51,63–70]. The results demonstrate that  $\{P_2W_{18}\}@Co\text{-BTC}$  is a promising electrode material.

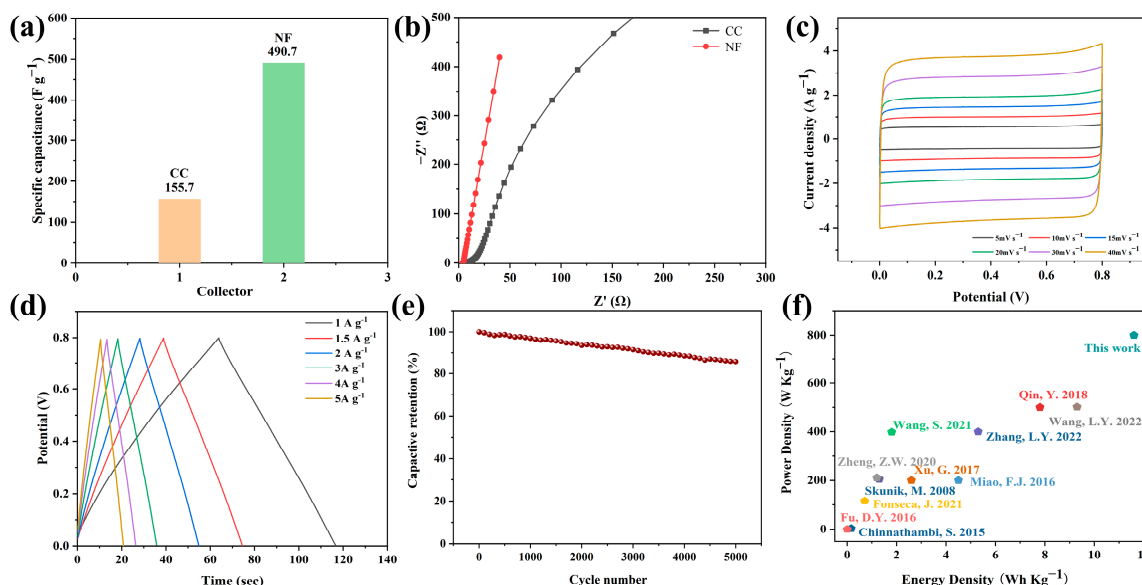


**Figure 5.** The specific capacitance (a) and EIS (b) in CC or NF as collector; the CV (c), GCD (d) and stability after 5000 cycles (e), Ragone plot (f) of  $\{P_2W_{18}\}@Co\text{-BTC}$  in double-electrode system [32,38,51,63–70].

### 3.3. $H_2O_2$ Sensor Performance

Here,  $\{P_2W_{18}\}@Co\text{-BTC}$  synthesized by the optimal ratio was selected as the electrode material, and the glassy carbon electrode was used as the collector (referred to as  $\{P_2W_{18}\}@Co\text{-BTC-GCE}$ ). Figure S14a is the CV curve of  $\{P_2W_{18}\}@Co\text{-BTC-GCE}$  at a scan rate of  $50 \text{ mV s}^{-1}$ . Two pairs of redox peaks with an average peak potential of  $-0.216$  and  $-0.519 \text{ V}$  (Equation (S5)) can be observed, which are related to the occurrence of one-electron and two-electron reduction processes for the  $\{P_2W_{18}\}$  anion [71]. Figure 6a shows the CV curves of  $\{P_2W_{18}\}@Co\text{-BTC-GCE}$  at different scan rates at  $-0.9$ – $0.5 \text{ V}$ . With an increase in the scan rate, the cathodic peak shifts to negative potential and the anodic peak shifts to positive potential [72]. Furthermore, Figure S14b shows that both the oxidation and reduction peak currents of  $\{P_2W_{18}\}@Co\text{-BTC-GCE}$  are positively correlated with the scan rate, implying that this nanomaterial is also a surface-controlled redox process in  $H_2O_2$  sensing. In order to test the catalytic activity of  $\{P_2W_{18}\}@Co\text{-BTC-GCE}$ ,  $H_2O_2$  solutions with concentrations of 0, 5, 10, 20, 30 and 40 mM were added under continuous stirring conditions, and the response current increased significantly with an increase in  $H_2O_2$  concentration. In addition, the cathodic peak current also increased correspondingly, suggesting that it has a good effect on the reduction of  $H_2O_2$  and good catalytic activity (Figure S14c) [73].

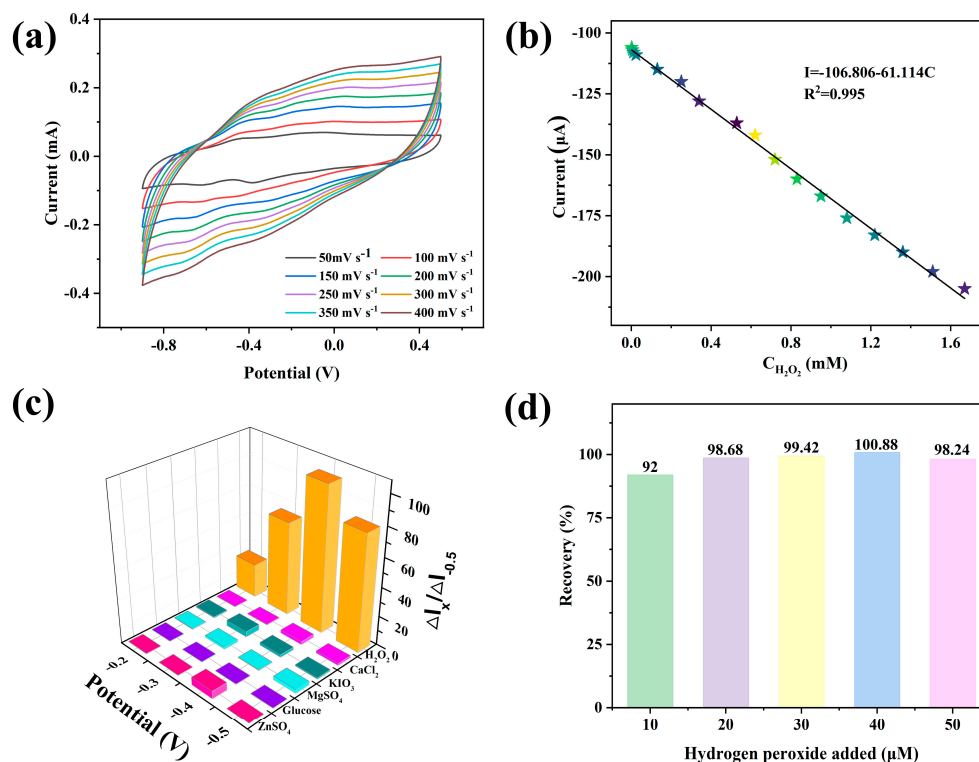


**Figure 6.** (a) CV curve of  $\{P_2W_{18}\}@Co-BTC-GCE$  at different scan rates; (b) calibration curve between the current response of  $\{P_2W_{18}\}@Co-BTC-GCE$  and the concentration of  $H_2O_2$ ; (c) the effects of different interferences on the sensor response; (d) the recovery values of  $H_2O_2$  in human serum was detected by  $\{P_2W_{18}\}@Co-BTC-GCE$  sensor.

The sensing performance of a nanomaterial is closely related to its sensitivity and detection limit, so we performed the current–time (*i-t*) test at the maximum response voltage. Figure S14d is the *i-t* curve of  $\{P_2W_{18}\}@Co-BTC-GCE$  during the continuous addition of  $H_2O_2$ . It can be found that the increasing speed of the response current increases with the increase in  $H_2O_2$  concentration [74,75]. Figure 6b is the standard curve of the current response of the title nanomaterial as a function of  $H_2O_2$  concentration. According to the figure, when  $\{P_2W_{18}\}@Co-BTC-GCE$  was used as the electrochemical sensor to detect  $H_2O_2$ , the linear equations were  $I(\mu A) = -106.806 - 61.114 C(mM)$  and  $R^2 = 0.995$  and the detection limit was  $0.633 \mu M$  ( $S/N = 3$ ). The sensitivity was  $8.65 mA mM^{-1} cm^{-2}$  and the total linear range was  $1.9 \mu M \sim 1.67 mM$ , superior to literature reports [76–79]. The linear range may be due to the large specific surface area and porosity of the POMOF core–shell structure, which facilitates the homogeneous dispersion of precursors and the transfer of electrons to the internal structure, thereby improving the reaction kinetics on the surface of the electrode material [80].

$CaCl_2$ ,  $MgSO_4$ ,  $ZnSO_4$ ,  $KIO_3$  and glucose solutions were used to examine the anti-interference and selectivity of  $\{P_2W_{18}\}@Co-BTC-GCE$ . Figure 6c shows a comparison of the current responses of the nanomaterials and the above five interfering agents at different voltages. Two phenomena can be observed: first, the catalytic current of the nanomaterials for  $H_2O_2$  is the most obvious regardless of the voltage tested; second, among the interfering substances,  $\{P_2W_{18}\}@Co-BTC-GCE$  has a weak current response to  $ZnSO_4$ , and other substances respond weakly. These results indicate that  $\{P_2W_{18}\}@Co-BTC-GCE$  has a good anti-interference ability and selectivity [81]. Meanwhile, the CV cycling curve was tested at  $40 mV s^{-1}$  to examine the stability of  $\{P_2W_{18}\}@Co-BTC-GCE$  (Figure S15). After 1000 cycles, the shape and peak value of the curve minimally change, and the retention rate of  $\{P_2W_{18}\}@Co-BTC-GCE$  is 92.4%, proving its excellent cycling stability.

To verify whether the sensor is promising for practical applications, real serum samples were selected for hydrogen peroxide content analysis. After diluting the serum samples 20 times with 0.1 M PBS (pH = 7.0) buffer solution, the samples of different concentrations were analyzed by the instrument, and the recovery values were calculated to be between 92.00 and 100.88% (Figure 6d), showing that  $\{P_2W_{18}\}@Co\text{-BTC-GCE}$  has a certain practical application prospect [82,83].

#### 4. Conclusions

A  $\{P_2W_{18}\}@Co\text{-BTC}$  nanomaterial with a molar ratio of 1:3 between  $CoK_4[P_2W_{18}O_{62}]$  and Co-BTC was prepared using the solid-phase grinding method, which has a lower resistance, better stability and higher specific capacitance. For the three-electrode system, the specific capacitance of  $\{P_2W_{18}\}@Co\text{-BTC}$  with nickel foam as the collector was higher than that of  $CoK_4[P_2W_{18}O_{62}]$  (215.4 F g<sup>-1</sup>), Co-BTC (106.5 F g<sup>-1</sup>), the physical mixture (99.6 F g<sup>-1</sup>) and  $\{P_2W_{18}\}@Co\text{-BTC-n}$ , which was greater than that when carbon cloth was the collector (155.7 F g<sup>-1</sup>). Furthermore, compared to  $CoK_4[P_2W_{18}O_{62}]$  (78.1%) and Co-BTC (87.8%),  $\{P_2W_{18}\}@Co\text{-BTC}$  has the best stability (90.6%). The  $\{P_2W_{18}\}@Co\text{-BTC}$  was assembled into a water-symmetric supercapacitor with a success rate and energy density of 800.00 W kg<sup>-1</sup> and 11.36 Wh kg<sup>-1</sup>, respectively. The results of H<sub>2</sub>O<sub>2</sub> sensing also show that  $\{P_2W_{18}\}@Co\text{-BTC-GCE}$  has a wide linear range (1.9 μM~1.67 mM), low detection limit (0.633 μM) and high stability (92.4%), as well as a good anti-interference ability and selectivity to CaCl<sub>2</sub>, MgSO<sub>4</sub>, ZnSO<sub>4</sub>, KIO<sub>3</sub> and glucose solutions. Moreover, sensors prepared from this material can be used to analyze H<sub>2</sub>O<sub>2</sub> in human serum samples. In summary, the Dawson-type nanomaterials synthesized using solid-phase grinding have bifunctional properties, which provide a new strategy for the synthesis of Dawson-type POMOFs and expand their application prospects in supercapacitors and H<sub>2</sub>O<sub>2</sub> sensing.

**Supplementary Materials:** The supporting information can be downloaded at <https://www.mdpi.com/article/10.3390/nano13071176/s1>, Figure S1: (a) The IR spectrum of Co-BTC,  $CoK_4[P_2W_{18}O_{62}]$ ,  $\{P_2W_{18}\}@Co\text{-BTC-n}$  (n=0, 1~3) and physical mixture; (b) The XRD of  $\{P_2W_{18}\}@Co\text{-BTC-n}$  (n=0, 1~3), Figure S2: The XPS full spectrum (a) and high-resolution of P<sub>2p</sub> (b), W<sub>4f</sub> (c), Co<sub>2p</sub> (d), K<sub>2p</sub> (e), O<sub>1s</sub> (f) and C<sub>1s</sub> (g) in  $\{P_2W_{18}\}@Co\text{-BTC}$ , Figure S3: The XPS full spectrum (a) and high-resolution of P<sub>2p</sub> (b), W<sub>4f</sub> (c), Co<sub>2p</sub> (d), K<sub>2p</sub> (e) and O<sub>1s</sub> (f) in  $CoK_4[P_2W_{18}O_{62}]$ , Figure S4: The XPS full spectrum (a) and high-resolution of Co<sub>2p</sub> (b), C<sub>1s</sub> (c) and O<sub>1s</sub> (d) in Co-BTC, Figure S5: The TG of  $\{P_2W_{18}\}@Co\text{-BTC}$ , Figure S6: EDS (a) and EDX spectra of C (b), O (c), K (d) of  $\{P_2W_{18}\}@Co\text{-BTC}$ , Figure S7: The SEM (a, b), EDX (c) and mapping (d) of  $CoK_4[P_2W_{18}O_{62}]$ , Figure S8: The SEM (a), EDS (b), EDX (c) and mapping (d) of Co-BTC, Figure S9: The BET (a) and pore size distribution map (b) of  $\{P_2W_{18}\}@Co\text{-BTC}$ ,  $CoK_4[P_2W_{18}O_{62}]$ , Co-BTC, Figure S10: (a) The CV of  $\{P_2W_{18}\}@Co\text{-BTC}$  in 40 mV s<sup>-1</sup>; (b) CV of  $CoK_4[P_2W_{18}O_{62}]$  and (c) Co-BTC at three-electrode system; (d) The  $\{P_2W_{18}\}@Co\text{-BTC}$ ,  $CoK_4[P_2W_{18}O_{62}]$ , Co-BTC plots of the anodic peak currents vs. scan rates; (e) Comparison diagram of GCD for  $\{P_2W_{18}\}@Co\text{-BTC}$ ,  $CoK_4[P_2W_{18}O_{62}]$ , Co-BTC and physical mixture; (f) The EIS of  $\{P_2W_{18}\}@Co\text{-BTC}$ ,  $CoK_4[P_2W_{18}O_{62}]$ , Co-BTC before and after 5000 cycles of the three electrodes system in the high-frequency region, Figure S11: The CV of  $\{P_2W_{18}\}@Co\text{-BTC}$  with CC (a) and NF (b) as collectors; (c) The CV of  $\{P_2W_{18}\}@Co\text{-BTC}$  in 40 mV s<sup>-1</sup> with CC as collector; (d) Comparison of GCD under the condition of current density of 1A g<sup>-1</sup>, CC and NF as collectors, Figure S12: The aqueous symmetric supercapacitor, Figure S13: The EIS of  $\{P_2W_{18}\}@Co\text{-BTC}$  before and after 5000 cycles of the symmetric double-electrode system (the insert is an enlarged view of the curves in the high-frequency region), Figure S14: (a) The 50 mV s<sup>-1</sup> CV of  $\{P_2W_{18}\}@Co\text{-BTC-GCE}$ ; (b) Linear curve of  $\{P_2W_{18}\}@Co\text{-BTC-GCE}$  oxidation-reduction peak (II) current as a function of scan rate; (c) The CV curves of electrocatalytic reduction of H<sub>2</sub>O<sub>2</sub> by  $\{P_2W_{18}\}@Co\text{-BTC-GCE}$ ; (d) The *i-t* curve of  $\{P_2W_{18}\}@Co\text{-BTC-GCE}$  with successive additions of H<sub>2</sub>O<sub>2</sub>, Figure S15: Cyclic stability (1000 cycles) for  $\{P_2W_{18}\}@Co\text{-BTC-GCE}$ , Table S1:  $\{P_2W_{18}\}$  part of the literature summary [23,25–32,34–36,39,41,58,63,78,84–93], Table S2: Atomic percent (%) of corresponding samples by ICP-MS analysis, Table S3: Performance comparison of Dawson-based materials with published polyoxometalate supercapacitors [19,23,27–31,39,63,94–106].

**Author Contributions:** Experimental feasibility investigation, L.Z.; writing—original draft, L.Z.; data verification and storage, S.D.; investigation, H.L.; validation, C.W. (Chunxiao Wang); formal analysis, K.Y.; methodological evaluation, J.L.; visualization of data, C.W. (Chunmei Wang); experimental conceptualization, B.Z.; writing—review and editing, B.Z. All authors have read and agreed to the published version of the manuscript.

**Funding:** This research was funded by the National Natural Science Foundation of China (22171061 and 21771046), the 2020 Central Government's Plan to Support the Talent Training Project of the Reform and Development Fund of Local Universities (2020GSP03), the Natural Science Foundation of Heilongjiang Province of China (ZD2021B002), the Master's Degree Candidate Innovation Project of Harbin Normal University (Grant HSDSSCX2022-112).

**Data Availability Statement:** The data presented in this study are available on request from the corresponding author.

**Conflicts of Interest:** The authors declare no conflict of interest.

## References

1. Zhang, Y.Z.; Wang, Y.; Cheng, T.; Yao, L.Q.; Li, X.; Lai, W.Y.; Huang, W. Printed supercapacitors: Materials, printing and applications. *Chem. Soc. Rev.* **2019**, *48*, 3229–3264. [[CrossRef](#)] [[PubMed](#)]
2. Shao, Y.; El-Kady, M.F.; Sun, J.; Li, Y.; Zhang, Q.; Zhu, M.; Wang, H.; Dunn, B.E.; Kaner, R.B. Design and Mechanisms of Asymmetric Supercapacitors. *Chem. Rev.* **2018**, *118*, 9233–9280. [[CrossRef](#)]
3. Liu, C.; Li, F.; Ma, L.P.; Cheng, H.M. Advanced Materials for Energy Storage. *Adv. Mater.* **2010**, *22*, E28–E62. [[CrossRef](#)] [[PubMed](#)]
4. Tian, Y.; Chang, Z.H.; Wang, X.L.; Lin, H.Y.; Zhang, Y.C.; Liu, Q.Q.; Chen, Y.Z. Pseudocapacitance improvement of polymolybdates-based metal-organic complexes via modification with hydrogen molybdenum bronze by electrochemical treatment. *Chem. Eng. J.* **2022**, *428*, 132380. [[CrossRef](#)]
5. Mustaqeem, M.; Naikoo, G.A.; Yarmohammadi, M.; Pedram, M.Z.; Pourfarzad, H.; Dar, R.A.; Taha, S.A.; Hassan, I.U.; Bhat, M.Y.; Chen, Y.F. Rational design of metal oxide based electrode materials for high performance supercapacitors—A review. *J. Energy Storage* **2022**, *55*, 105419. [[CrossRef](#)]
6. Peng, Z.K.; Liu, X.; Meng, H.; Li, Z.J.; Li, B.J.; Liu, Z.Y.; Liu, S.C. Design and Tailoring of the 3D Macroporous Hydrous RuO<sub>2</sub> Hierarchical Architectures with a Hard-Template Method for High-Performance Supercapacitors. *ACS Appl. Mater. Interfaces* **2017**, *9*, 4577–4586. [[CrossRef](#)] [[PubMed](#)]
7. Bagal, I.V.; Chodankar, N.R.; Waseem, A.; Johar, M.A.; Patil, S.J.; Abdullah, A.; Hassan, M.A.; Han, Y.K.; Ryu, S.W. CF<sub>4</sub> plasma-treated porous silicon nanowire arrays laminated with MnO<sub>2</sub> nanoflakes for asymmetric pseudocapacitors. *Chem. Eng. J.* **2021**, *419*, 129515. [[CrossRef](#)]
8. Qiu, M.J.; Sun, P.; Shen, L.X.; Wang, K.; Song, S.Q.; Yu, X.; Tan, S.Z.; Zhao, C.X.; Mai, W.J. WO<sub>3</sub> nanoflowers with excellent pseudo-capacitive performance and the capacitance contribution analysis. *J. Mater. Chem. A* **2016**, *4*, 7266–7273. [[CrossRef](#)]
9. Mahmood, Q.; Kim, W.S.; Park, H.S. Structure and compositional control of MoO<sub>3</sub> hybrids assembled by nanoribbons for improved pseudocapacitor rate and cycle performance. *Nanoscale* **2012**, *4*, 7855–7860. [[CrossRef](#)]
10. Barbieri, O.; Hahn, M.; Herzog, A.; Kotz, R. Capacitance limits of high surface area activated carbons for double layer capacitors. *Carbon* **2005**, *43*, 1303–1310. [[CrossRef](#)]
11. Liu, T.Y.; Liu, G.L. Block copolymer-based porous carbons for supercapacitors. *J. Mater. Chem. A* **2019**, *7*, 23476–23488. [[CrossRef](#)]
12. Lobato, B.; Suárez, L.; Guardia, L.; Centeno, T.A. Capacitance and surface of carbons in supercapacitors. *Carbon* **2017**, *122*, 434–445. [[CrossRef](#)]
13. Cui, L.P.; Yu, K.; Lv, J.H.; Guo, C.H.; Zhou, B.B. 3D POMOF based on {AsW<sub>12</sub>} cluster and Ag-MOF with interpenetrating channels for large-capacity aqueous asymmetric supercapacitors and highly selective biosensors detecting hydrogen peroxide. *J. Mater. Chem. A* **2020**, *8*, 22918–22928. [[CrossRef](#)]
14. Yang, K.; Ying, Y.X.; Cui, L.L.; Sun, J.C.; Luo, H.; Hu, Y.Y.; Zhao, J.W. Stable aqueous Zn–Ag and Zn–polyoxometalate hybrid battery driven by successive Ag<sup>+</sup> cation and polyoxoanion redox reactions. *Energy Storage Mater.* **2021**, *34*, 203–210. [[CrossRef](#)]
15. Liu, J.C.; Wang, J.F.; Han, Q.; Guan, P.S.; Liu, L.L.; Chen, L.J.; Zhao, J.W.; Streb, C.; Song, Y.F. Multicomponent Self-Assembly of a Giant Heterometallic Polyoxotungstate Supercluster with Antitumor Activity. *Angew. Chem. Int. Ed.* **2021**, *60*, 11153–11157. [[CrossRef](#)] [[PubMed](#)]
16. Zhu, J.J.; Hemesh, A.; Biendicho, J.J.; Soria, L.M.; Garcia, D.R.; Morante, J.R.; Ballesteros, B.; Romero, P.G. Rational design of MXene/activated carbon/polyoxometalate triple hybrid electrodes with enhanced capacitance for organic-electrolyte supercapacitors. *J. Colloid Interface Sci.* **2022**, *623*, 947–961. [[CrossRef](#)]
17. Hou, Y.; Chai, D.F.; Li, B.N.; Pang, H.J.; Ma, H.Y.; Wang, X.M.; Tan, L.C. Polyoxometalate-Incorporated Metallacalixarene@Graphene Composite Electrodes for High-Performance Supercapacitors. *ACS Appl. Mater. Interfaces* **2019**, *11*, 20845–20853. [[CrossRef](#)] [[PubMed](#)]

18. Wang, X.; Li, H.; Lin, J.F.; Wang, C.Y.; Wang, X.L. Capped Keggin Type Polyoxometalate-Based Inorganic–Organic Hybrids Involving In Situ Ligand Transformation as Supercapacitors and Efficient Electrochemical Sensors for Detecting Cr(VI). *Inorg. Chem.* **2021**, *60*, 19287–19296. [[CrossRef](#)]
19. Zhu, J.J.; Vilaua, R.B.; Romero, P.G. Can polyoxometalates enhance the capacitance and energy density of activated carbon in organic electrolyte supercapacitors? *Electrochim. Acta* **2020**, *362*, 137007. [[CrossRef](#)]
20. Roy, S.; Vemuri, V.; Maiti, S.; Manoj, K.S.; Subbarao, U.; Peter, S.C. Two Keggin-Based Isostructural POMOF Hybrids: Synthesis, Crystal Structure, and Catalytic Properties. *Inorg. Chem.* **2018**, *57*, 12078–12092. [[CrossRef](#)]
21. Yang, M.H.; Choi, B.G.; Jung, S.C.; Han, Y.K.; Huh, Y.S.; Lee, S.B. Polyoxometalate-coupled Graphene via Polymeric Ionic Liquid Linker for Supercapacitors. *Adv. Funct. Mater.* **2014**, *24*, 7301–7309. [[CrossRef](#)]
22. Du, N.N.; Gong, L.G.; Fan, L.Y.; Yu, K.; Luo, H.; Pang, S.J.; Gao, J.Q.; Zheng, Z.W.; Lv, J.H.; Zhou, B.B. Nanocomposites Containing Keggin Anions Anchored on Pyrazine-Based Frameworks for Use as Supercapacitors and Photocatalysts. *ACS Appl. Nano Mater.* **2019**, *2*, 3039–3049. [[CrossRef](#)]
23. Wang, G.N.; Chen, T.T.; Li, S.B.; Pang, H.J.; Ma, H.Y. A coordination polymer based on dinuclear (pyrazinyl tetrazolate) copper(II) cations and Wells–Dawson anions for high-performance supercapacitor electrodes. *Dalton Trans.* **2017**, *46*, 13897–13902. [[CrossRef](#)]
24. Fang, P.T.; Lu, X.M.; Zhou, Q.; Yan, D.X.; Xin, J.Y.; Xu, J.L.; Shi, C.Y.; Zhou, Y.Q.; Xia, S.Q. Controlled alcoholysis of PET to obtain oligomers for the preparation of PET-PLA copolymer. *Chem. Eng. J.* **2023**, *451*, 138988. [[CrossRef](#)]
25. Hong, B.; Liu, L.; Wang, S.M.; Han, Z.B. Facile Synthesis of ZIF-8/ZnO/Polyoxometalate Ternary Composite Materials for Efficient and Rapid Removal of Cationic Organic Dye. *J. Clust. Sci.* **2016**, *27*, 563–571. [[CrossRef](#)]
26. Li, J.P.; Wu, D.; Wang, C.L.; Liu, D.; Chen, W.L.; Wang, X.L.; Wang, E.B. Interfacial self-assembly engineering for constructing a 2D flexible superlattice polyoxometalate/rGO heterojunction for high-performance photovoltaic devices. *Dalton Trans.* **2020**, *49*, 3766–3774. [[CrossRef](#)]
27. Yang, A.S.; Cui, L.P.; Yu, K.; Lv, J.H.; Ma, Y.J.; Zhao, T.T.; Zhou, B.B. Supramolecular Host–Guest Assembly Based on Phosphotungstate Nanostructures for Pseudocapacitive and Electrochemical Sensing Applications. *ACS Appl. Nano Mater.* **2022**, *5*, 10452–10461. [[CrossRef](#)]
28. He, L.L.; Cui, L.P.; Yu, K.; Lv, J.H.; Ma, Y.J.; Tian, R.; Zhou, B.B. The pseudocapacitance and sensing materials constructed by Dawson/basket-like phosphomolybdate. *J. Solid State Chem.* **2022**, *316*, 123578. [[CrossRef](#)]
29. Tian, R.; Cui, L.P.; Yu, K.; Lv, J.H.; Ma, Y.J.; He, L.L.; Zhou, B.B. Arsenotungstate-Nanostructure-Based Derivatives with One-Dimensional Tunnels for Electrochemical Capacitors and Electrocatalytic Hydrogen Evolution. *ACS Appl. Nano Mater.* **2022**, *5*, 14882–14892. [[CrossRef](#)]
30. Zhong, R.; Cui, L.P.; Yu, K.; Lv, J.H.; Guo, Y.H.; Zhang, E.M.; Zhou, B.B. Wells–Dawson Arsenotungstate Porous Derivatives for Electrochemical Supercapacitor Electrodes and Electrocatalytically Active Materials. *Inorg. Chem.* **2021**, *60*, 9869–9879. [[CrossRef](#)]
31. Gao, J.Q.; Gong, L.G.; Fan, X.Y.; Yu, K.; Zheng, Z.W.; Zhou, B.B. {P<sub>2</sub>W<sub>18</sub>O<sub>62</sub>}-Encapsulated Potassium-Ion Nanotubes Intercalated in Copper Bimidazole Frameworks for Supercapacitors and Hydrogen Peroxide Sensing. *ACS Appl. Nano Mater.* **2020**, *3*, 1497–1503. [[CrossRef](#)]
32. Fonseca, J.; Gong, T.H.; Jiao, L.; Jian, H.L. Metal–organic frameworks (MOFs) beyond crystallinity: Amorphous MOFs, MOF liquids and MOF glasses. *J. Mater. Chem. A* **2021**, *9*, 10562. [[CrossRef](#)]
33. Sheberla, D.; Bachman, J.C.; Elias, J.S.; Sun, C.J.; Horn, Y.S.; Dinc, M. Conductive MOF electrodes for stable supercapacitors with high areal capacitance. *Nat. Mater.* **2017**, *16*, 220–224. [[CrossRef](#)]
34. Yang, X.Y.; Li, M.T.; Sheng, N.; Li, J.S.; Liu, G.D.; Sha, J.Q.; Jiang, J.Z. Structure and LIBs Anode Material Application of Novel Wells–Dawson Polyoxometalate-Based Metal Organic Frameworks with Different Helical Channels. *Cryst. Growth Des.* **2018**, *18*, 5564–5572. [[CrossRef](#)]
35. Lü, Y.; Xiao, L.N.; Hao, X.R.; Cui, X.B.; Xu, J.Q. A series of organic–inorganic hybrid compounds formed by [P<sub>2</sub>W<sub>18</sub>O<sub>62</sub>]<sup>6-</sup> and several types of transition metal complexes. *Dalton Trans.* **2017**, *46*, 14393–14405. [[CrossRef](#)] [[PubMed](#)]
36. Fan, X.Y.; Guo, H.; Lv, J.H.; Yu, K.; Su, Z.H.; Wang, L.; Wang, C.M.; Zhou, B.B. Efficient and robust photocatalysts based on {P<sub>2</sub>W<sub>18</sub>} modified by Ag complex. *Dalton Trans.* **2018**, *47*, 4273–4281. [[CrossRef](#)]
37. Cong, B.W.; Su, Z.H.; Zhao, Z.F.; Wang, B. A novel 3D POMOFs based on Wells–Dawson arsenomolybdates with excellent photocatalytic and lithium-ion batteries performance. *CrystEngComm* **2017**, *19*, 7154–7161. [[CrossRef](#)]
38. Qin, Y.; Kong, X.G.; Lei, D.Q.; Lei, X.D. Facial Grinding Method for Synthesis of High-Purity CuS Nanosheets. *Ind. Eng. Chem. Res.* **2018**, *57*, 2759–2764. [[CrossRef](#)]
39. Liang, Y.; Di, S.; Wang, C.M.; Yu, K.; Wang, C.X.; Lv, J.H.; Zhou, B.B. Synthesis of {P<sub>2</sub>W<sub>18</sub>}-based coated structured nano materials with supercapacitors and H<sub>2</sub>O<sub>2</sub> sensing. *J. Energy Storage* **2022**, *56*, 105991. [[CrossRef](#)]
40. Liang, C.Y.; Wang, X.; Yu, D.X.; Guo, W.; Zhang, F.; Qu, F.Y. In-situ immobilization of a polyoxometalate metal-organic framework (NENU-3) on functionalized reduced graphene oxide for hydrazine sensing. *Chin. J. Chem.* **2021**, *39*, 2889–2897. [[CrossRef](#)]
41. Chen, Y.; Yao, Z.X.; Miras, H.N.; Song, Y.F. Modular Polyoxometalate-Layered Double Hydroxide Composites as Efficient Oxidative Catalysts. *Chem. Eur. J.* **2015**, *21*, 10812–10820. [[CrossRef](#)]
42. Lu, H.S.; Bai, L.L.; Xiong, W.W.; Li, P.Z.; Ding, J.F.; Zhang, G.D.; Wu, T.; Zhao, Y.L.; Lee, J.M.; Yang, Y.H.; et al. Surfactant Media To Grow New Crystalline Cobalt 1,3,5-Benzenetricarboxylate Metal–Organic Frameworks. *Inorg. Chem.* **2014**, *53*, 8529–8537. [[CrossRef](#)] [[PubMed](#)]

43. Li, H.X.; Wan, J.Q.; Ma, Y.W.; Wang, Y.; Chen, X.; Guan, Z.Y. Degradation of refractory dibutyl phthalate by peroxymonosulfate activated with novel catalysts cobalt metal-organic frameworks: Mechanism, performance, and stability. *J. Hazard. Mater.* **2016**, *318*, 154–163. [[CrossRef](#)] [[PubMed](#)]
44. Sun, Z.; Duan, X.X.; Zhao, J.; Wang, X.L.; Jiang, Z.J. Homogeneous borotungstic acid and heterogeneous micellar borotungstic acid catalysts for biodiesel production by esterification of free fatty acid. *Biomass Bioenergy* **2015**, *76*, 31–42. [[CrossRef](#)]
45. Lü, Y.Y.; Zhan, W.W.; He, Y.; Wang, Y.T.; Kong, X.J.; Kuang, Q.; Xie, Z.X.; Zheng, L.S. MOF-templated synthesis of porous  $\text{Co}_3\text{O}_4$  concave nanocubes with high specific surface area and their gas sensing properties. *ACS Appl. Mater. Interfaces* **2014**, *6*, 4186–4195. [[CrossRef](#)]
46. Chae, I.S.; Kim, M.; Kang, Y.S.; Kang, S.W. Enhanced  $\text{CO}_2$  carrier activity of potassium cation with fluorosilicate anions for facilitated transport membranes. *J. Membr. Sci.* **2014**, *466*, 357–360. [[CrossRef](#)]
47. Dong, Y.Y.; Zhang, J.; Yang, Y.L.; Wang, J.Q.; Hu, B.Y.; Wang, W.; Cao, W.; Gai, S.; Xia, D.B.; Lin, K.F.; et al. Multifunctional nanostructured host-guest POM@MOF with lead sequestration capability induced stable and efficient perovskite solar cells. *Nano Energy* **2022**, *97*, 107184. [[CrossRef](#)]
48. Shreyanka, S.N.; Theerthagiri, J.; Lee, S.J.; Yu, Y.; Choi, M.Y. Multiscale design of 3D metal-organic frameworks (M-BTC, M: Cu, Co, Ni) via PLAL enabling bifunctional electrocatalysts for robust overall water splitting. *Chem. Eng. J.* **2022**, *446*, 137045. [[CrossRef](#)]
49. Tang, Y.J.; Chen, Y.F.; Zhu, H.J.; Zhang, A.M.; Wang, X.L.; Dong, L.Z.; Li, S.L.; Xu, Q.; Lan, Y.Q. Solid-Phase Hot-Pressing Synthesis of POMOFs on Carbon Cloth and Derived Phosphides for All pH Values Hydrogen Evolution. *J. Mater. Chem. A* **2018**, *6*, 21969–21977. [[CrossRef](#)]
50. Li, C.; Lou, X.B.; Shen, M.; Hu, X.S.; Guo, Z.; Wang, Y.; Hu, B.W.; Chen, Q. High Anodic Performance of Co<sub>1,3,5</sub>-Benzenetricarboxylate Coordination Polymers for Li-Ion Battery. *ACS Appl. Mater. Interfaces* **2016**, *8*, 15352–15360. [[CrossRef](#)]
51. Wang, L.Y.; Kang, N.; Gong, L.G.; Wang, C.X.; Yu, K.; Wang, C.M.; Zhou, B.B. A novel core-shell structured hybrid composed of zinc homobenzotriazolate and silver borotungstate with supercapacitor and photocatalytic dye degradation performance. *J. Energy Storage* **2022**, *46*, 103873. [[CrossRef](#)]
52. Zhong, X.H.; Lu, Y.; Luo, F.; Liu, Y.W.; Li, X.H.; Liu, S.X. A nanocrystalline POM@MOFs catalyst for the degradation of phenol: Effective cooperative catalysis by metal nodes and POM guests. *Chem. Eur. J.* **2018**, *24*, 3045–3051. [[CrossRef](#)]
53. Gautam, J.; Liu, Y.; Gu, J.; Ma, Z.Y.; Dahal, B.; Chishti, A.N.; Ni, L.B.; Diao, G.W.; Wei, Y.G. Three-dimensional nano assembly of nickel cobalt sulphide/polyaniline@polyoxometalate/reduced graphene oxide hybrid with superior lithium storage and electrocatalytic properties for hydrogen evolution reaction. *J. Colloid Interface Sci.* **2022**, *614*, 642–654. [[CrossRef](#)] [[PubMed](#)]
54. Chai, D.F.; Garcias, C.J.G.; Li, B.N.; Pang, H.J.; Ma, H.Y.; Wang, X.M.; Tan, L.C. Polyoxometalate-based metal-organic frameworks for boosting electrochemical capacitor performance. *Chem. Eng. J.* **2019**, *373*, 587–597. [[CrossRef](#)]
55. Yang, K.; Hu, Y.Y.; Li, L.Y.; Cui, L.L.; He, L.; Wang, S.J.; Zhao, J.W.; Song, Y.F. First high-nuclearity mixed-valence polyoxometalate with hierarchical interconnected  $\text{Zn}^{2+}$  migration channels as an advanced cathode material in aqueous zinc-ion battery. *Nano Energy* **2020**, *74*, 104851. [[CrossRef](#)]
56. Oliveira, R.D.; Santos, C.S.; Garcia, J.R.; Vidotti, M.; Marchesi, L.F.; Pessoa, C.A. IR drop studies of poly(aniline)-based modified electrodes. *J. Electroanal. Chem.* **2020**, *878*, 114662. [[CrossRef](#)]
57. Wang, D.W.; Wang, Y.T.; Liu, H.W.; Xu, W.; Xu, L. Unusual carbon nanomesh constructed by interconnected carbon nanocages for ionic liquid-based supercapacitor with superior rate capability. *Chem. Eng. J.* **2018**, *342*, 474–483. [[CrossRef](#)]
58. Boussema, F.; Grossa, A.J.; Hmida, F.; Ayed, B.; Majdoub, H.; Cosnier, S.; Maaref, A.; Holzinger, M. Dawson-type polyoxometalate nanoclusters confined in a carbon nanotube matrix as efficient redox mediators for enzymatic glucose biofuel cell anodes and glucose biosensors. *Biosens. Bioelectron.* **2018**, *109*, 20–26. [[CrossRef](#)]
59. Shinde, P.A.; Khan, M.F.; Rehman, M.A.; Jung, E.; Pham, Q.N.; Won, Y.; Jun, S.C. Nitrogen-doped carbon integrated nickel-cobalt metal phosphide marigold flowers as a high capacity electrode for hybrid supercapacitors. *CrystEngComm* **2020**, *22*, 6360. [[CrossRef](#)]
60. Li, X.; Rong, J.P.; Wei, B.Q. Electrochemical behavior of single-walled carbon nanotube supercapacitors under compressive stress. *ACS Nano* **2010**, *4*, 6039–6049. [[CrossRef](#)]
61. Qiu, Y.F.; Dai, X.F.; Wang, Y.P.; Ji, X.Y.; Ma, Z.; Liu, S.Q. The polyoxometalates mediated preparation of phosphate-modified  $\text{NiMoO}_{4-x}$  with abundant O-vacancies for  $\text{H}_2$  production via urea electrolysis. *J. Colloid Interface Sci.* **2023**, *629*, 297–309. [[CrossRef](#)] [[PubMed](#)]
62. Zhao, L.; Lei, S.J.; Tu, Q.Y.; Rao, L.H.; Zen, W.H.; Xiao, Y.H.; Cheng, B.C. Phase-controlled growth of nickel hydroxide nanostructures on nickel foam for enhanced supercapacitor performance. *J. Energy Storage* **2021**, *43*, 103171. [[CrossRef](#)]
63. Chinnathambi, S.; Ammam, M. A molecular hybrid polyoxometalate-organometallic moieties and its relevance to supercapacitors in physiological electrolytes Selvaraj Chinnathambi. *J. Power Source* **2015**, *284*, 524–535. [[CrossRef](#)]
64. Wang, S.; Wang, X.; Sun, C.L.; Wu, Z.S. Room-temperature fast assembly of 3D macroscopically porous graphene frameworks for binder-free compact supercapacitors with high gravimetric and volumetric capacitances. *J. Energy Chem.* **2021**, *61*, 23–28. [[CrossRef](#)]
65. Skunik, M.; Chojak, M.; Rutkowska, I.A.; Kulesza, P.J. Improved capacitance characteristics during electrochemical charging of carbon nanotubes modified with polyoxometalate monolayers. *Electrochim. Acta* **2008**, *53*, 3862–3869. [[CrossRef](#)]

66. Zheng, Z.W.; Zhao, X.Y.; Gong, L.G.; Wang, C.X.; Wang, C.M.; Yu, K.; Zhou, B.B. Coral-like  $\{\text{SiW}_{10}\text{Mn}_2\}$ -based Mn-MOFs: Facile fabrication with high electrochemical capacitor performance. *J. Solid State Chem.* **2020**, *288*, 121409. [CrossRef]
67. Fu, D.Y.; Li, H.W.; Zhang, X.M.; Han, G.Y.; Zhou, H.H.; Chang, Y.Z. Flexible solid-state supercapacitor fabricated by metal-organic framework/graphene oxide hybrid interconnected with PEDOT. *Mater. Chem. Phys.* **2016**, *179*, 166–173. [CrossRef]
68. Miao, F.J.; Shao, C.L.; Li, X.H.; Wang, K.X.; Lu, N.; Liu, Y.C. Three-dimensional freestanding hierarchically porous carbon materials as binder-free electrodes for supercapacitors: High capacitive property and long-term cycling stability. *J. Mater. Chem. A* **2016**, *4*, 5623–5631. [CrossRef]
69. Li, W.H.; Ding, K.; Tian, H.R.; Yao, M.S.; Nath, B.; Deng, W.H.; Wang, Y.B.; Xu, G. Conductive Metal–Organic Framework Nanowire Array Electrodes for High-Performance Solid-State Supercapacitors. *Adv. Funct. Mater.* **2017**, *27*, 1702067. [CrossRef]
70. Zhang, L.Y.; Zhao, X.Y.; Wang, C.M.; Yu, K.; Lv, J.H.; Wang, C.X.; Zhou, B.B. The supercapacitor and photocatalytic supermolecule materials constructed by 4'-pyridine and  $\{\text{PMo}_{12}\text{O}_{40}\}$ . *J. Solid State Chem.* **2022**, *312*, 123235. [CrossRef]
71. Liang, Y.; Kang, N.; Wang, C.M.; Yu, K.; Lv, J.H.; Wang, C.X.; Zhou, B.B. A hybrid of borotungstate-coated metal-organic framework with supercapacitance, photocatalytic dye degradation and  $\text{H}_2\text{O}_2$  sensing properties. *Dalton Trans.* **2022**, *51*, 7613–7621.
72. Li, X.; Sun, L.J.; Yang, X.Y.; Zhou, K.F.; Zhang, G.G.; Tong, Z.B.; Wang, C.; Sha, J.Q. Enhancing colorimetric detection of  $\text{H}_2\text{O}_2$  and ascorbic acid on polypyrrole coating fluconazole functionalized POMOFs. *Analyst* **2019**, *144*, 3347–3356. [CrossRef]
73. Zhou, W.; Huang, S.; Sun, C.G.  $\text{Ni}_3\text{Mo}_3\text{N}$  coupled with nitrogen-rich carbon microspheres as an efficient hydrogen evolution reaction catalyst and electrochemical sensor for  $\text{H}_2\text{O}_2$  detection. *Int. J. Hydrogen Energy* **2022**, *47*, 14906–14915. [CrossRef]
74. Wang, Q.Q.; Zhang, X.M.; Chai, X.Y.; Wang, T.Q.; Cao, T.L.; Li, Y.N.; Zhang, L.Y.; Fan, F.Q.; Fu, Y.; Qi, W. An Electrochemical Sensor for  $\text{H}_2\text{O}_2$  Based on Au Nanoparticles Embedded in UiO-66 Metal–Organic Framework Films. *ACS Appl. Nano Mater.* **2021**, *4*, 6103–6110. [CrossRef]
75. Li, W.W.; Liu, J.; Chen, C.; Zhu, Y.D.; Liu, N.; Zhou, Y.M.; Chen, S.R. High catalytic performance non-enzymatic  $\text{H}_2\text{O}_2$  sensor based on  $\text{Cu}_2\text{O}@\text{Cu}_9\text{S}_5$  yolk-shell nanospheres. *Appl. Surf. Sci.* **2022**, *587*, 152766. [CrossRef]
76. Sun, C.X.; Ying, J.; Zhang, Y.P.; Jin, L.; Tian, A.X.; Wang, X.L. A series of POM-based compounds by tuning coordination groups and spacers of ligands: Electrocatalytic, capacitive and photoelectrocatalytic properties. *CrystEngComm* **2022**, *24*, 587–600. [CrossRef]
77. Jin, L.; Ying, J.; Zhang, Y.P.; Sun, C.X.; Tian, A.X.; Wang, X.L. A series of polyoxometalate compounds by tuning N sites and numbers of ligands: Syntheses, characterization and electrochemical sensing, and photocatalytic and supercapacitor properties. *New J. Chem.* **2022**, *46*, 8422. [CrossRef]
78. Zhu, H.T.; Du, J.; Lu, Y.; Su, F.; Li, Y.G. Immobilization of enzymes on an organic–inorganic hybrid network consisting of Dawson-type polyoxotungstate and a zinc(II)-imidazole complex moiety. *New J. Chem.* **2019**, *43*, 146–153. [CrossRef]
79. Kong, X.X.; Shen, Q.Q.; Wan, T.T.; Li, K.Y.; Sun, F.G.; Wu, H.L. Two silver(I) complexes: Synthesis, structures, and electrochemical  $\text{H}_2\text{O}_2$  sensing. *J. Chin. Chem. Soc.* **2022**, *69*, 540–548. [CrossRef]
80. Liu, Q.Q.; Lu, J.J.; Lin, H.Y.; Wang, X.L.; Chang, Z.H.; Chen, Y.Z.; Zhang, Y.C. Polyoxometalate-based metal–organic complexes constructed from a new bispyrimidine-amide ligand with high capacitance performance and selectivity for the detection of Cr(VI). *Chin. Chem. Lett.* **2022**, *33*, 4389–4394. [CrossRef]
81. Dong, Y.H.; Zheng, J.B. Environmentally friendly synthesis of Co-based zeolitic imidazolate framework and its application as  $\text{H}_2\text{O}_2$  sensor. *Chem. Eng. J.* **2020**, *392*, 123690. [CrossRef]
82. Zhao, T.T.; Cui, L.P.; Yu, K.; Lv, J.H.; Ma, Y.J.; Yang, A.S.; Zhou, B.B. Porous  $\{\text{P}_6\text{Mo}_{18}\text{O}_{73}\}$ -type Poly(oxometalate) Metal–Organic Frameworks for Improved Pseudocapacitance and Electrochemical Sensing Performance. *ACS Appl. Mater. Interfaces* **2022**, *24*, 30099–30111. [CrossRef] [PubMed]
83. Chen, Y.; Li, F.B.; Li, S.B.; Zhang, L.; Sun, M. A review of application and prospect for polyoxometalate-based composites in electrochemical sensor. *Inorg. Chem. Commun.* **2022**, *235*, 109084. [CrossRef]
84. Ammar, S.H.; Salman, M.D.; Shafi, R.F. Keggin- and Dawson-type polyoxotungstates immobilized on poly(3, 4-ethylenedioxythiophene)-coated zerovalent iron nanoparticles: Synthesis, characterization and their catalytic oxidative desulfurization activity. *J. Environ. Chem. Eng.* **2021**, *9*, 104904. [CrossRef]
85. Shi, N.; Liu, D.; Dang, F.L.; Chen, Q.T.; Li, M.; Wen, F.S. Bifunctional and recyclable Dawson-type polyoxometalates catalyze oxidative degradation of lignocellulose to selectively produce phthalates. *Bioresour. Technol.* **2019**, *273*, 677–681. [CrossRef] [PubMed]
86. Shan, Y.P.; Yang, G.C.; Jia, Y.T.; Gong, J.; Su, Z.M.; Qu, L.Y. ITO electrode modified with chitosan nanofibers loading polyoxometalate by one step self-assembly method and its electrocatalysis. *Electrochem. Commun.* **2007**, *9*, 2224–2228. [CrossRef]
87. Chi, Y.N.; Cui, F.Y.; Lin, Z.G.; Xu, Y.; Ma, X.Y.; Shen, P.P.; Huang, K.L.; Hu, C.W. Assembly of Cu/Ag-quinoxaline-polyoxotungstate hybrids: Influence of Keggin and Wells–Dawson polyanions on the structure. *J. Solid State Chem.* **2013**, *199*, 230–239. [CrossRef]
88. Wang, R.X.; Liu, Y.F.; Zuo, P.; Zhang, Z.D.; Lei, N.N.; Liu, Y.Q. Phthalocyanine-sensitized evolution of hydrogen and degradation of organic pollutants using polyoxometalate photocatalysts. *Environ. Sci. Pollut. Res.* **2020**, *27*, 18831–18842. [CrossRef]
89. Zheng, X.T.; Chen, W.L.; Chen, L.; Wang, Y.J.; Guo, X.W.; Wang, J.B.; Wang, E.B. A strategy for breaking polyoxometalate-based MOFs to obtain high loading amount of nanosized polyoxometalate clusters to improve the performance of dye-sensitized solar cells. *Chem. Eur. J.* **2017**, *23*, 8871–8878. [CrossRef]
90. Liu, S.P.; Xu, L.; Li, F.Y.; Guo, W.H.; Xing, Y.; Sun, Z.X. Carbon nanotubes-assisted polyoxometalate nanocomposite film with enhanced electrochromic performance. *Electrochim. Acta* **2011**, *56*, 8156–8162. [CrossRef]

91. Xing, R.M.; Tong, L.Y.; Zhao, X.Y.; Liu, H.L.; Ma, P.T.; Zhao, J.W.; Liu, X.Q.; Liu, S.H. Rapid and sensitive electrochemical detection of myricetin based on polyoxometalates/SnO<sub>2</sub>/gold nanoparticles ternary nanocomposite film electrode. *Sens. Actuators B Chem.* **2019**, *283*, 35–41. [[CrossRef](#)]
92. Mu, A.Q.; Li, J.S.; Chen, W.L.; Sang, X.J.; Su, Z.M.; Wang, E.B. The composite material based on Dawson-type polyoxometalate and activated carbon as the supercapacitor electrode. *Inorg. Chem. Commun.* **2015**, *55*, 149–152. [[CrossRef](#)]
93. Guan, Y.; Cui, L.P.; Yu, K.; Lv, J.H.; Deng, Y.F.; Wang, C.M.; Zhou, B.B. Two arsenic capped Dawson-type supramolecular hybrid assemblies induced by benzimidazole for photo-/electro-catalytic performance. *J. Solid State Chem.* **2020**, *292*, 121707. [[CrossRef](#)]
94. Hou, Y.; Pang, H.J.; Gómez-García, C.J.; Ma, H.Y.; Wang, X.M.; Tan, L.C. Polyoxometalate Metal–Organic Frameworks: Keggin Clusters Encapsulated into Silver-Triazole Nanocages and Open Frameworks with Supercapacitor Performance. *Inorg. Chem.* **2019**, *58*, 16028–16039. [[CrossRef](#)]
95. Chai, D.F.; Hou, Y.; O’Halloran, K.P.; Pang, H.J.; Ma, H.Y.; Wang, G.N.; Wang, X.M. Enhancing Energy Storage via TEA-Dependent Controlled Syntheses: Two Series of Polyoxometalate-Based Inorganic–Organic Hybrids and their Supercapacitor Properties. *Chem. Electro. Chem.* **2018**, *5*, 3443–3450. [[CrossRef](#)]
96. Gallegos, A.K.C.; Cantú, M.L.; Pastor, N.C.; Romero, P.G. Nanocomposite Hybrid Molecular Materials for Application in Solid-State Electrochemical Supercapacitors. *Adv. Funct. Mater.* **2015**, *15*, 1125–1133. [[CrossRef](#)]
97. Guevara, J.S.; Ruiza, V.; Romero, P.G. Stable graphene–polyoxometalate nanomaterials for application in hybrid supercapacitors. *Phys. Chem. Chem. Phys.* **2014**, *16*, 20411–20414. [[CrossRef](#)]
98. Hu, C.C.; Zhao, E.B.; Nitta, N.; Magasinski, A.; Bardichevsky, G.; Yushin, G. Aqueous solutions of acidic ionic liquids for enhanced stability of polyoxometalate-carbon supercapacitor electrodes. *J. Power Sources* **2016**, *326*, 569–574. [[CrossRef](#)]
99. Genovese, M.; Lian, K. Polyoxometalate modified pine cone biochar carbon for supercapacitor electrodes. *J. Mater. Chem. A* **2017**, *5*, 3939–3947. [[CrossRef](#)]
100. Dubal, D.P.; Chodankar, N.R.; Vinu, A.; Kim, D.H.; Gomez-Romero, P. Asymmetric Supercapacitors Based on Reduced Graphene Oxide with Different Polyoxometalates as Positive and Negative Electrodes. *ChemSusChem* **2017**, *10*, 2742–2750. [[CrossRef](#)]
101. Mohamed, A.M.; Ramadan, M.; Ahmed, N.; ElNaga, A.O.A.; Alalawy, H.H.; Zaki, T.; Shaban, S.A.; Hassan, H.B.; Allam, N.K. Metal–Organic frameworks encapsulated with vanadium-substituted heteropoly acid for highly stable asymmetric supercapacitors. *J. Energy Storage* **2020**, *28*, 101292. [[CrossRef](#)]
102. Li, T.Y.; He, P.; Dong, Y.N.; Chen, W.C.; Wang, T.; Gong, J.; Chen, W.L. Polyoxometalate-Based Metal–Organic Framework/Polypyrrole Composites toward Enhanced Supercapacitor Performance. *Eur. J. Inorg. Chem.* **2021**, *21*, 2063–2069. [[CrossRef](#)]
103. Quezada, E.F.; Casillas, D.C.M.; Gallegos, A.K.C.; Llave, E.d.l. Effect of Hierarchical Porosity on PMo<sub>12</sub> Adsorption and Capacitance in Hybrid Carbon–PMo<sub>12</sub> Electrodes for Supercapacitors. *Energy Fuels* **2022**, *36*, 3987–3996. [[CrossRef](#)]
104. Hu, S.M.; Li, K.Q.; Yu, X.J.; Jin, Z.X.; Xiao, B.X.; Yang, R.R.; Pang, H.J.; Ma, H.Y.; Wang, X.M.; Tan, L.C.; et al. Enhancing the electrochemical capacitor performance of Keggin polyoxometalates by anchoring cobalt-triazole complexes. *J. Mol. Struct.* **2022**, *1250*, 131753. [[CrossRef](#)]
105. Hou, Y.J.; Han, P.L.; Zhang, L.K.; Li, H.; Xu, Z.H. pH-controlled assembling of POM-based metal–organic frameworks for use as supercapacitors and efficient oxidation catalysts for various sulfides. *Inorg. Chem. Front.* **2023**, *10*, 148–157. [[CrossRef](#)]
106. Yu, X.J.; Khan, S.U.; Jin, Z.X.; Wu, Q.; Pang, H.J.; Ma, H.Y.; Wang, X.M.; Tan, L.C.; Yang, G.X. Water cluster encapsulated polyoxometalate-based hydrogen-bonded supramolecular frameworks (PHSFs) as a new family of high-capacity electrode materials. *J. Energy Storage* **2022**, *53*, 105192. [[CrossRef](#)]

**Disclaimer/Publisher’s Note:** The statements, opinions and data contained in all publications are solely those of the individual author(s) and contributor(s) and not of MDPI and/or the editor(s). MDPI and/or the editor(s) disclaim responsibility for any injury to people or property resulting from any ideas, methods, instructions or products referred to in the content.